Contract # NASW-4854

PROGRESS REPORT

Venus Surface Roughness and Magellan Stereo Data

Prepared by

K.E. Maurice, F.W. Leberl, L. Norikane
Vexcel Corporation, Boulder, Colorado

and

S. Hensley
Jet Propulsion Laboratory, Pasadena California

Submitted to

NASA CASI, NASA HQ

Vexcel Corporation
2477 55th Street
Boulder, Colorado 80301

14 September 1994

ABSTRACT

Presented are results of some studies to develop tools useful for the analysis of Venus surface shape and roughness. Actual work was focused on Maxwell Montes. The analyses employ data acquired by means of NASA's Magellan satellite. The work is primarily concerned with deriving measurements of the Venusian surface using Magellan stereo SAR. Roughness was considered by means of a theoretical analyses based on Digital Elevation Models (DEMs), on single Magellan radar images combined with radiometer data, and on the use of multiple overlapping Magellan radar images from Cycles I, II and III, again combined with collateral radiometer data. The goal is to develop tools and methods to support the generation of planetary surface roughness maps. Such maps can be used to infer information about the ages of volcanic units through the use of erosion, weathering and deposition process models. The generation of roughness information requires precise knowledge of the terrain slopes as well as calibrated images showing SAR backscatter clean of the effects of slope and dielectric constants. We focus here on methods for surface shape measurements. We discuss data issues and show numerical descriptions of surface shape. The subsequent derivation of roughness has only been defined theoretically. Implementation and assessment of accuracy will remain the subject of future work.

TABLE OF CONTENTS

1. INTRODUCTION

Surface roughness of planet Venus from NASA's Magellan Mission is an important element in the analysis of Venus geology [Arvidson et al., in press]. NASA's Magellan satellite has of course produced a tremendous wealth of roughly 4000 radar image strips about the planet's surface, but it also generated surface topographic measurements by means of radar altimetry, observed the surface's emmissivity through radiometer observations and performed sophisticated gravity measurements [Saunders, et al., 1992; Pettengill, et al., 1991]. This collection of data has provided scientists with information useful in modeling many of the geophysical and geologic processes on Venus; it has been speculated that this data exceeds the quality and completeness of similar data sets currently available about our planet Earth [Leberl et. al., 1991].

The roughness of the surface can be defined in terms of detail at a continental or global scale, or it can address the local small scale variations over areas in the meter or centimeter range. "Roughness" is a property of the terrain that is either described as a root mean square variation of elevations in a given area, or as a root mean square variation of slopes. One has the dimension of length, the other of angle. While the global or continental scale assessment of roughness may be based on altimeter and stereo-based topographic Digital Elevation Models (DEMs), it becomes an issue of examining each individual pixel to derive observations of local surface characteristics. However, this analysis requires that accurate high-resolution topographic models be developed in an area of interest, that SAR images be calibrated, and that radiometric information be included in the analysis. The use of stereo imagery offers significant support for this type of analysis. This leads to topographic shape information and enhances the interpretability and usefulness of the original data sets. Derived data products can be defined and will provide a critical input to the detailed study of surface characteristics and to conclusions about important geologic and geomorphologic parameters such as the age of lava flows.

We will focus in the following report on the technologies currently available and applicable to the Magellan full-resolution image data, either in the form of individual products of each orbit, the so-called F-BIDRs, or in the form of derived mosaicked F-MIDRs. We will discuss the currently available and implemented methods to measure the surface shape and to extract from it the roughness of a surface on a global or continental scale as well as methods for sub-radar-wavelength measurements.

The combination of such DEMs with the source images leads to radiometrically modified images which have the effects of surface slope removed from the image's brightness data. We describe a method to accomplish such a product, with complete implementation, as yet, ongoing.

The resulting DEM can be used to describe, in terms of slopes, the "roughness" of the surface modeled in the DEM. However, this is not of great interest. Significant is the question of the local surface roughness within the area covered by a single image pixel of size 75 m x 75 m. Methods to address this local roughness include the consideration of dielectric properties of the surface within a pixel, and attempt to exclude the effects of this property on the image pixel's brightness. We will discuss the theoretical model under which this dielectric property can be modeled and removed from an image. The resulting product will represent the radar reflections as affected by surface roughness.

1.1 Approach Based on Stereopsis

In [Tyler and Simpson 1992], [Senske et al. 1992] and elsewhere it has been pointed out that large scale slope data are available from Magellan altimetry. However, high-resolution terrain information is only available through stereo techniques while repeat track interferometry is a promising method for surface shape reconstruction, but is not supported by the Magellan data set. As [Farr et al. 1993] report, about 21% of the surface of Venus has been imaged in stereo, offering an opportunity to not only generate high precision topographic maps but to also create geometrically and, more importantly, radiometrically corrected image products. Images from which the radar reflection effects due to terrain slope have been removed are called here "calibrated". Such calibrated images provide backscatter data that are essentially a function only of the small scale surface roughness and the dielectric constant of the surface's material. As [Arvidson et al., in print] and others have pointed out, Venus is a planet with considerably intriguing dielectric properties of surface materials. Stereo-derived topo data can support analysis of these properties.

The focus of our effort has so far been to produce DEMs of high accuracy and resolution from stereo images, depending on the limitations imposed by Magellan's imaging geometry and quality. These DEMs are used to correct image geometric and radiometric distortions due to terrain, following the model proposed by [Curlander 1991], [Rignot,

1992] or [Bayer et al. 1991]. Included in these corrections should be normalizations for SAR processor errors due to original Pioneer Venus and antenna pattern projections as well as the use of the specific model of Muhlman's incidence angle dependence.

The DEM results in a "calibrated" image which can be the basis of surface roughness estimates at each pixel. Separately, the DEM itself is a source for computing revised surface roughnesses. We will discuss in Section 5 the case of the DEM improving the SAR images, and in Section 6 the estimation of roughness parameters.

We differentiate between two Magellan stereo-processing schemes. One is based on mosaicked images (F-MIDRs) and employs many approximations; the concern exists that the approximations invalidate the usefulness of the resulting DEMs for all but the most localized studies. The other scheme is based on the original range-Doppler observations of the SAR system and promises superior accuracy; however, the methodology and processing system must still need to be put in place and verified.

As previous studies have shown, SAR images can be employed for so-called "model inversion"; the resulting surface power spectra help to date lava flows. On Earth such data were used by [Evans et al. 1992], [van Zyl et al. 1991] and [Farr 1992] to establish surface roughness. Transferring these methods to Venus will require a determination of detailed topography and an appropriate theoretical model.

1.2 Approach Based on Surface Radiometry

Magellan radiometer data are to be used to infer dielectric constants for individual lava flow units. A simplified view of the relationship between (Fresnel) reflectivity ρ and dielectric constant ε is given by [Farr et. al. 1993] as:

$$\rho = \left| \frac{1-\sqrt{\varepsilon}}{1+\sqrt{\varepsilon}} \right|^2 \qquad (1)$$

where we can then obtain an approximate value of emissivity as $e = 1 - \rho$, where e is the (average) emissivity. This dependence is in turn removed from image pixels to leave only roughness-dependent scattering in the SAR image data. These reduced images can

We also have refined the DEMs from F-MIDRs using various implementations of so-called shape-from-shading. However, in an effort to differentiate surface units by means of different surface backscatter properties, shape-from-shading needs to be employed very judiciously. Its use presupposes knowledge of surface backscatter, a factor we seek to determine. Therefore we speculate that shape-from-shading can only then be used for this task if we manage to employ three overlapping images with strongly disparate incidence angles. We will therefore need to deal with all three Magellan Cycles I, II and III in one joint analysis effort to resolve the ambiguities between surface slope, dielectric constant and surface roughness. Shape-from-shading is thus a process element for associating with each pixel a slope estimate, and integrating these estimates into an elevation model, while other process elements resolve the issue of dielectric and roughness properties.

At the current time we have not implemented a system to employ three images. We also still need to add radiometry data to the image analysis.

2. TOPOGRAPHIC SHAPE RECONSTRUCTION METHODS

2.1 Terrain Models for Planetary Studies

In past planetary missions the major source of terrain elevation data was altimetry. This is in itself a method of elevation measurement which is robust only when the surface is flat, such as with ocean surfaces on Earth. As soon as topographic relief becomes accentuated, altimetric echoes will be ambiguous and the resulting DEM will be inaccurate. This will be particularly distinct in the description of relatively small features such as volcanoes, craters, steep mountain ridges etc. [Leberl et al. 1991] have found examples of altimetric observations over such features that are in error by $\pm$ 1 km or more. In addition altimetry observations are typically feasible at large intervals of some kilometers only, leading to a DEM with widely spaced postings. While Magellan produced a Global Topographic Data Record (GTDR) with a spacing of ~5 km, this is not the true spacing of independent observations. These are in the range of perhaps 13 km and more, and support the interpolation of a regular grid of topographic elevations.

Magellan's image coverage supports the use of stereopsis to extract DEMs at accuracies of $\pm$ 100 m, and thus will permit one to describe the surface elevations by a grid with a mesh size of perhaps 500 m [see Leberl et. al., 1992]. This can be used for detailed

analyses of surface characteristics such as small steep slopes, stability of the surface, etc. As [Arvidson et al., in press] have argued, such detailed knowledge of the surface shape also permits one to unravel the surprising brightness variations in radar images which may be caused by temperature changes on the surface as a function of terrain elevation. These analyses need accuracies of relative elevation differences in the range of 100 to 300 meters.

A separate issue is the measurement of slopes over rather short vertical ranges of, say, 300 meters. These have been the subject of work by [Connors, in preparation]. Many of the slopes are close to the incidence angle of the radar system and get therefore fully compressed into 1 or several pixels. As a result, a stereo matching process will not work to measure such slopes. We will discuss alternate methods as used by [Connors, in preparation] or [Leberl et al. 1991].

In summary we have a number of data sources for extracting topographic information of Venus at various scales and locations. Some products already exist and can be directly used (such as altimetry) while others must be derived using stereopsis or radarclinometry (shape-from-shading) as described below.

2.2 Stereo-Methods for Creating Topographic Data of Venus

The stereo algorithms used in this study include those employed in conventional mapping as well as those found in 3rd-party image processing software packages. We utilize 3-D techniques of stereo reconstruction as well as simplified geometric methods.

Two packages were used for elevation and DEM-processing, a system to process full resolution image strips per orbit, F-BIDRs, developed at JPL (Figure 1) [Hensley and Shaffer, 1994] and the Magellan Stereo Toolkit (Figure 2) [Vexcel Corp., 1994], for approximate computations based initially on mosaicked products (F-MIDRs).

We thus use two techniques to reconstruct terrain, one based on F-BIDR data [JPL, 1990] and one based on F-MIDR data [JPL, 1991b]. The first technique uses a detailed ephemeris and range-Doppler stereo intersection [Hensley and Shaffer, 1994], [Leberl, 1990], [Dowman et. al., 1992]. The second employs a nominal ephemeris and simplified parallax computations to build the height models [Leberl et. al, 1992]. It would be possible to incorporate detailed imaging geometry and accurate navigational data into the

simplified parallax computations. However, the relationship between mosaicked image products and the radar system's detailed bursts of radiation is a detour that can be avoided when starting from F-BIDRs.

Different methods have been proposed in the literature to make elevation measurements using overlapping stereo radar images. Authors include [Welch 1992], [Schanda 1985], [Leberl, 1990] and others. For the present study we compare two methods of differing complexity:

least squares range-Doppler stereo intersection with detailed ephemeris and navigational corrections

versus

approximate parallax computation using a nominal ephemeris and no navigation corrections.

Since the process based on F-BIDRs has previously not been described in any detail except for [Hensley and Shaffer, 1994], we will present additional details of the BIDR processes. In contrast, we have previously discussed the simplified process for parallax measurements with mosaicked F-MIDR data and therefore refer to that literature [Leberl, 1990], [Leberl et. al., 1992], [Vexcel Corp., 1994].

2.3 Using Overlapping F-BIDRs

We present stereo-processing software developed and utilized in this effort for F-BIDRs. While the F-BIDR-based process is separate from the Magellan Stereo Toolkit MST, it is compatible with it so that data can transferred into MST for visualization. Currently, the entire system consists of 4 parts: (a) reading of F-BIDRs; (b) image matching; (c) range-Doppler computing for the stereo intersection; (d) DEM gridding and image geocoding; a 5th part is being developed for radiometric correction of the ortho-image mosaics.

(a) Reading of F-BIDRs

This first software component has a largely administrative function and will not be further discussed. Details of reading and processing F-BIDRs can be found in documents of the Magellan mission [JPL, 1990].

(b) Image Matching

Image matching is the process that takes raw input images, both in the form of BIDRs or MIDRs, and produces correspondence image points for a feature found in two images. Due to the nature of radar imaging the stereo partners are rather dissimilar [Domik, 1984]; therefore it is useful that special methods be used to create useful overlapping stereo images. For matching by machine and for visual viewing one needs to constrain the imaging geometry to cases where the radiometric differences in the overlap areas are not excessive. [Domik, 1984] has described typical cases and specific imaging geometries that can be employed for optimal matching and fusing. The stereo imaging geometry adapted for Magellan was the result of an experiment during Cycle II of the mission [Leberl et al., 1992]. This suggested that the incidence angles or Desired Look Angle Profile (DLAP) for the second look at the surface be inside that of the initial look in Cycle I. This was in principle implemented, with the exception of the orbits passing over Maxwell Montes. There the initial look angles were very small since the feature is at a high geographic latitude. Therefore it made sense and was feasible to have the stereo mate be taken at a shallower look angle over Maxwell Montes. Detailed look angle profiles for these orbits were described in [Farr et. al., 1993].

The fundamental trade-off that must be made when matching Magellan images is that of speed vs. accuracy. While automated methods have been shown to compare with manual methods to within $\pm$ 2 pixels [Leberl et al., 1994], there remains a need to visually inspect and accept the automated matches. This is due to the possibility of outliers or blunders. Manual inspection of dense automated measurements presents in turn a new problem in that the manipulation and viewing of individual points from a set of perhaps millions becomes prohibitively difficult.

Image matching is a well-documented problem domain with extensive literature. We currently use two different matching algorithms. The Automatcher by [Frankot et. al. 1994] is a hierarchical matcher of square mixed arrays computing a correlation maximum and a measure of confidence for each match. The match locations are regular in one of the overlaying images.

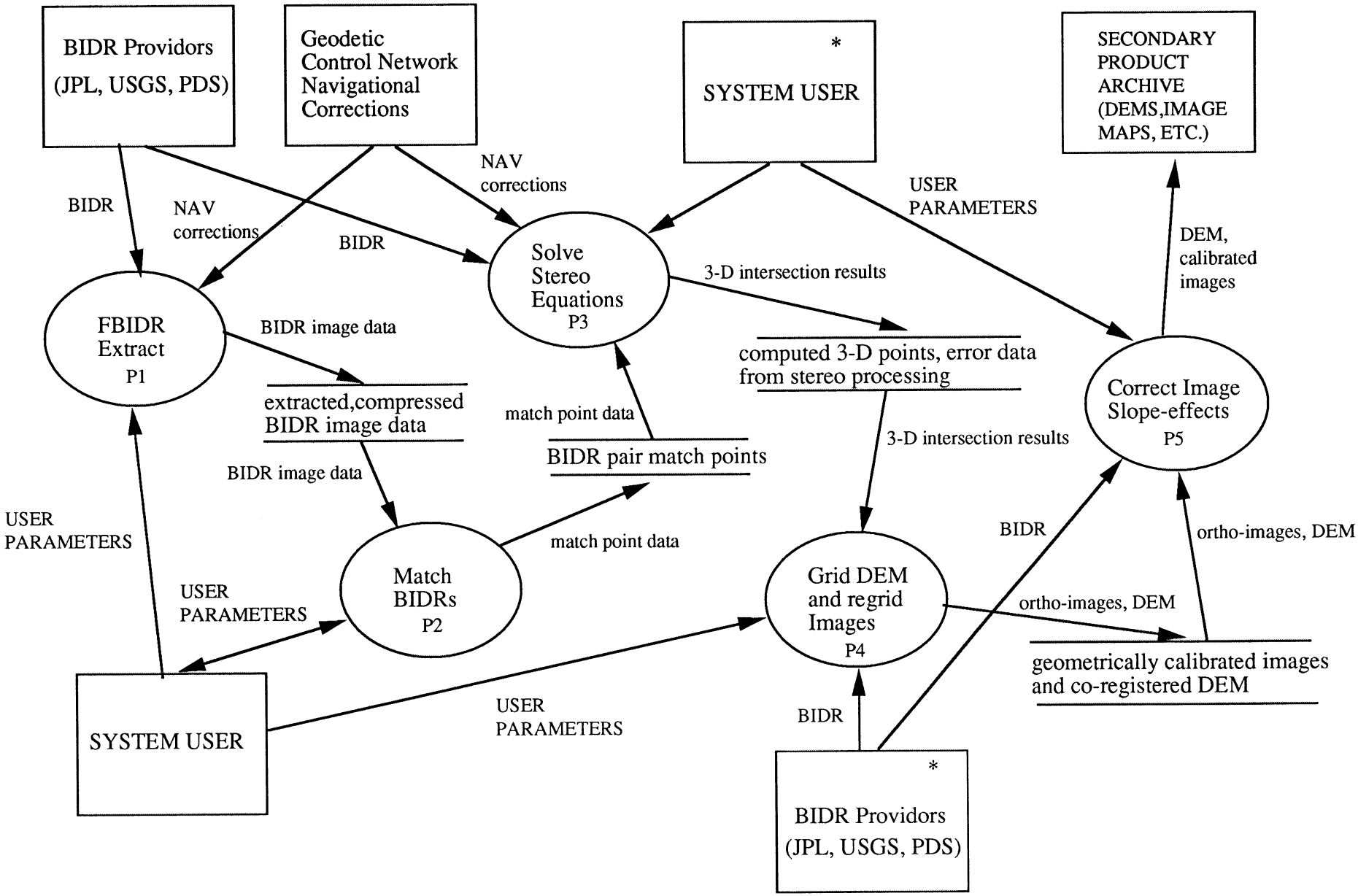

Figure 1.System Architecture for the F-BIDR Stereo Processing System. P1-P5 denote the program elements in the actual implementation.

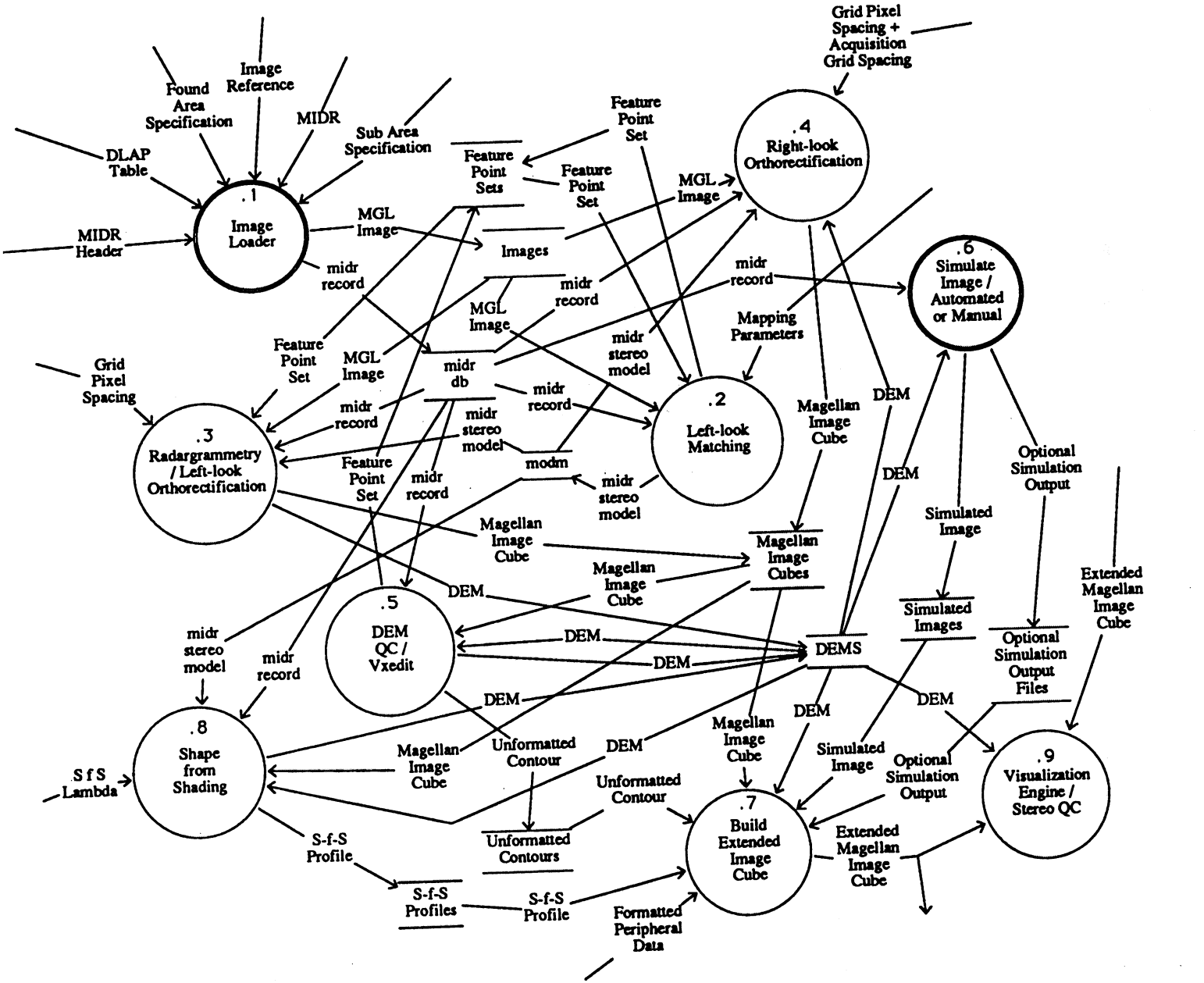

Figure 2.System Architecture for the F-MIDR Magellan Stereo Toolkit Kernal.

The second method by INRIA is feature-based, which searches for interesting image areas where strong matches are likely to occur. As a result, this method is robust where featureless areas may exist in the object.

The match method of Frankot-Hensley-Shaffer [Frankot et. al., 1994] attempts to monitor results dynamically using adaptive "robust" weighted least squares (RWLS) estimation that we believe eliminates most of the blunders leaving errors that are primarily at a noise level comparable to that which an experienced stereo operator will encounter.

A trade-off also exists between resolution of the feature to be captured by the matching process and matching errors introduced by noise in the images. After extensive evaluation we have concluded that matching can be performed optimally, for Magellan images, at a pixel spacing between 8 and 4 pixels, limited inherently by the signal strength of the multi-look image frames.

The measurement accuracy of stereoscopic manual collection is typically viewed as being one of the critical advantages of manual collection in that it offers the ability of an operator to "fuse" a 3-D surface and place a measuring mark as opposed to 2-D matching or automated methods which are relying on variations in the image gray values . While it is likely that the automated matching performance on specific data sets can be tuned to improve upon or even match the performance of manual collection, this remains a case by case process highly dependent on the scene and imaging parameters.

A significant limitation of stereo matching presents itself in highly compressed (foreshortened) slopes facing the antenna. Such slopes will become so narrow in one image that there is no texture that would permit a match with the second image to occur. However, it is these steep slopes that are often of specific interest and methods must be found to single out areas of such slopes which then could be reconstructed by machine using concepts such as those proposed by Connors (in preparation).

(c) Stereo Solution

This step takes measured image coordinate pairs in the F-BIDRs and converts them into measurements of slant range and Doppler frequency. Knowing the satellite's position and velocity leads to the computation of a circle in 3-D space in each image. The two circles

produce the terrain point at their intersection. The 3-D cartesian coordinates need then to be transformed into a sinusoidal projection. Each patch of overlapping F-BIDRs produces a "cloud" of points. The stereo equations for nonzero Doppler [Hensley and Shaffer, 1994], [Leberl, 1990] are

$$
\begin{aligned}
r_1^2 &= \langle \mathbf{T} - \mathbf{P}_1, \mathbf{T} - \mathbf{P}_1 \rangle \\
f_1 &= \frac{\langle \mathbf{T} - \mathbf{P}_1, \mathbf{V}_1 \rangle}{\lambda r_1} \\
r_2^2 &= \langle \mathbf{T} - \mathbf{P}_2, \mathbf{T} - \mathbf{P}_2 \rangle \\
f_2 &= \frac{\langle \mathbf{T} - \mathbf{P}_2, \mathbf{V}_2 \rangle}{\lambda r_2}
\end{aligned}
\qquad (2)
$$

since $\vec{R}_i = \vec{T} - \vec{P}$ and $r_i = \text{range}_i = |\vec{R}_i| = \sqrt{\langle \vec{T} - \vec{P}_i, \vec{T} - P_i \rangle}$.

Here **T** is the unknown position vector of the target scatterer with 3 elements, f_i is the Doppler frequency, r_i is the (observed) range to the target for each of the two orbits, $\mathbf{P}_i$ is the spacecraft position vector for each orbit, $\vec{R}_i$ is the pointing vector from sensor to target and λ is the radar wavelength; i = 1,2. We have 4 equations to solve for the 3 unknown elements of **T**.

Here again is a trade-off: the more rigorous F-BIDR-method requires greater data storage and processing requirements, and navigational corrections that may not be available. But the stereo solutions offer the most accurate possible results in terms of absolute and relative planimetric and height errors, while the approximate F-MIDR-solution remains robust, simple, easy-to-use and available across the large amounts of mosaic data already issued to the Magellan science community. However, its accuracy may be low considering the noticeably large positional errors in F-BIDRS which will lead to false stereo-parallaxes and elevation errors.

(d) DEM Gridding and Image Geometric Resampling

The point clouds per patch of overlapping F-BIDR images serve as the basis for the DEM which is obtained by interpolating the computed points onto a regular map projection

grid. The user controls the output grid spacing and coordinate window in producing the DEMs.

DEM gridding forms the resulting DEM by interpolating terrain elevations at regular, user-specified coordinate system spacings. The choice of grid-spacing is dependent on the match spacing and as a rule-of-thumb in mapping should be no greater than 3 times that of matching. For Magellan data of Venus however, due to the high-frequency terrain features found in many areas, we believe that this rule will not apply as strongly. In particular we have many highly foreshortened features. This should lead one to match as densely as possible, causing us to push the limits of matching to the 4-8 pixel level.

The gridding algorithm is based on the Akima method, which is widely available through the algorithm collections published by ACM [Akima, 1978]. This enforces continuity of first derivatives and integrability, important properties for roughness determination, given the requirement to work with slope and not elevation data. An additional property of use is that its interpolation model passes through each of the input points.

This process augments previously used Magellan gridding schemes by (i) managing the computation using small blocks of data and (ii) performing image resampling during the DEM gridding stage. Given that the locations of DEM points are known both in the input images as well as in the output XY-coordinate system, it was seen to be an appropriate place to actually interpolate the image gray values for each input image. This process therefore produces a DEM in a user-specified output projection along with co-registered and geometrically calibrated SAR images.

These geometrically corrected images will also have to be radiometrically corrected for the effect of the now-known slope of the terrain.

2.4 Using Overlapping F-MIDRs

F-MIDR products were designed to relieve the scientist from working with the complex and storage intensive F-BIDR products. Thus the thin orbital strips of 300 x 220 pixels are replaced with mosaics from multiple orbit swaths. The overhead of manipulating stereo models of entire planet-long strips in order to process aggregate areas on Venus using F-BIDRs is traded-off against a reduced accuracy and completeness of the mosaic products, however covering 8192 x 7168 pixels.

This stereo-process consists also of several steps as described in the following.

(a) Matching

Essentially the same algorithm described for F-BIDRs, modified to work on simple image pairs, is used to obtain matches for the F-MIDR pairs.

(b) Stereo Parallax

The match points produce parallax differences by assuming that the coordinates of the corner-points, as given, are correct (from so-called "dead-reckoning", using the nominal ephemeris) and thus allowing an absolute datum reference given that all images are projected onto the Pioneer Venus topo model. The emphasis is not to compute absolute elevations of the terrain, but rather to routinely determine the relative elevation differences with respect to the de facto datum point (which may be in error due to ephemeris uncertainty). The DEM should undergo a "calibration" step where it is leveled to other data (at least 3 points) such as altimetry or BIDR stereo.

The parallax differences are then simply converted into elevation differences by an equation which assumes known radar incidence angles, and it replaces the spherical wave front by its tangent plane. This approach is based on a number of simplifying approximations. Its DEM is that which would be produced from the more rigorous approach would the ephemeris be error free, at a constant orbit altitude at a constant look angle across the entire mosaic and without the spherical figure of the planet.

The stereo parallaxes represent the surface elevation above Pioneer Venus topomodel. To obtain the elevations above a spherical datum surface it is necessary to back in the topomodel.

As part of the mission's preparation for stereo data collection, an analysis of F-BIDR radar images evaluated parallaxes and concluded that cross track navigation errors can occur that cause up to 1 km error in the computation of height differences between points located in different F-BIDRs [Hensley, unpublished JPL-Mission material].

(c) Gridding and Resampling

A variant of Akima's algorithm is built into the image processing subsystem IDL (Research Systems Inc.) and is being used as part of MST. It is being employed to generate MST-based DEMs and to geocode or rectify the SAR images.

This F-MIDR related software differs from the F-BIDR gridding element, although both use Akima. MST's does not allow gridding of very large point sets encountered in typical Magellan stereo processing. The MST version is dependent on physical memory and has problems when processing point sets in excess of 50,000. This limit does not exist in the F-BIDR processing chains.

2.5 Using Altimetry

The direct measurement of terrain elevation is of course through altimetry. MST supports access to the global altimetric data from Magellan. This is the recommended data set for a broad overview of terrain elevations. Its validity is limited to areas of gradual topographic relief. In areas of topographic relief (where stereopsis is applicable), altimetry can produce erroneous elevation data, distorting particularly elevation profiles over features with delicate shapes such as volcanoes, craters and such.

Raw altimetry profiles as observed by the satellite and not yet processed through interpolation to create the global data set may contain information about small features such as craters. As [Leberl. et. al. 1991] have shown, this can, in combination with the radar images, lead to improved measurements of the elevation differences in craters and volcanoes. Access to raw altimetry echoes is through a separate software element denoted MGMDQE and available through the MIT Center for Space Research.

2.6 Shape from Shading

A promising technique for achieving maximum terrain model resolution is that which employs radarclinometry or "shape-from-shading" to interpolate stereo-derived height measurements using the input SAR images and the slopes obtained from the stereo data. MST contains a method, described by [Thomas et. al., 1991], that is an expansion of a method previously described by [Frankot and Chellapa, 1987]. It is currently implemented for a nominal ephemeris and has been tested extensively on MIDR

Magellan data. A number of improvements to this algorithm, however, have been identified.

The basic idea behind shape-from-shading is the hypothesis that an image grey value (digital number DN) is greatly dependent upon the incidence angle, and that therefore the incidence angle can be estimated from DN-values. Various authors have proposed algorithms to compute incidence angles, terrain slopes, and terrain elevations [Wildey, 1978; Kirk, 1987]. These do not typically employ multiple radar images, which can be easily merged in stereoscopic analysis of multiple images.

Shape from Shading (SfS) depends on an estimate of the surface backscatter properties, so that image brightness variations can be correctly interpreted as a result of slope variations of the terrain. The weakness of SfS is its inability to determine backscatter properties. Instead one simply must assume the backscatter characteristics in an often arbitrary manner and as a uniform item across the entire imaged area. The model used is either a cosine-reflectivity law or the reflection models proposed by [Muhleman, 1964] or [Hagfors, 1964], each with global parameterization chosen somewhat arbitrarily.

Major improvements may include not just single Muhleman's or Hagfors' backscatter constants but multiple constants that are input as masks into the imagery and cause associated lookup table elements to be referenced during reflectance map calculation.

The dielectric constants, derived from the radiometer data in a prior step, should be used in the above reflectance map computation.

The capability of SfS to utilize precise navigation information found in the F-BIDR processing parameters and employ a precisely computed look angle off-nadir to replace the simplification of a constant look angle is needed as a further improvement.

2.7 Other Methods

Direct monoscopic or multiple image methods exist for making spot elevation measurements. [Leberl. et. al., 1991] reviewed the methods in existence. These may include the use of the observable length of shadows or layovers, etc. It may exploit the knowledge that a feature such as a volcano or crater is symmetric, and that therefore the two opposite sides of the feature can be treated as if they were the two images of a stereo

pair. Another approach is non-stereo exploitation of overlapping images, as [Dalke and McCoy, 1968] have demonstrated, and as Connors (in preparation) is now using to determine the slopes of small features which cannot be matched in stereo.

3. DATA ISSUES

Our work focuses on a small number of areas that are of interest for their geometric and radiometric qualities and because of the availability of special orbital correction data. We plan to compare various types of topographic datasets that cover the areas. At this point we have only performed work on Maxwell Montes. However, the other areas remain on the list of things to do as resources permit.

3.1 Maxwell Montes, 65 North, 0 East

This area (Figure 3) has had extensive previous analysis due to interest in both its steep terrain and surface properties [Pettengill and Ford 1991], [Alexandrov et. al., 1986]. For this reason Maxwell Montes has been paid particular attention by the Magellan Mission as well as the Magellan Project in providing special orbital coverage, custom data processing and navigation ephemeris corrections. For this region, specific corrections were made to the navigation data, provided by research on the north pole control network [Davies et. al., 1992], and ephemeris refinement by [Chodas et. al., 1993], and applied during reprocessing of the basic image data products (BIDRs).

The select availability of these navigation corrections currently constrains the use of the most sophisticated and accurate methods of stereo solution to only Maxwell Montes.

The specific site is presented in Figure 4, using a portion of an F-MIDR stereo-pair.

3.2 Ovda Regio, 2 South, 74 East, 8 South 71 East

This area is considered part of Aphrodite Terra. The area under study has been imaged in stereo under the Stereo Experiment using images from Cycles I and II. Given its proximity to the equator it affords an opportunity to compare differences

Figure 3. Maxwell Montes Cycle 1 F–MIDR covering Latitudes 63.5 to 67.5 degrees and Longitudes 357.0 to 2.0 degrees, encompassing 240 km x 450 km and showing the study site in the enclosed box.

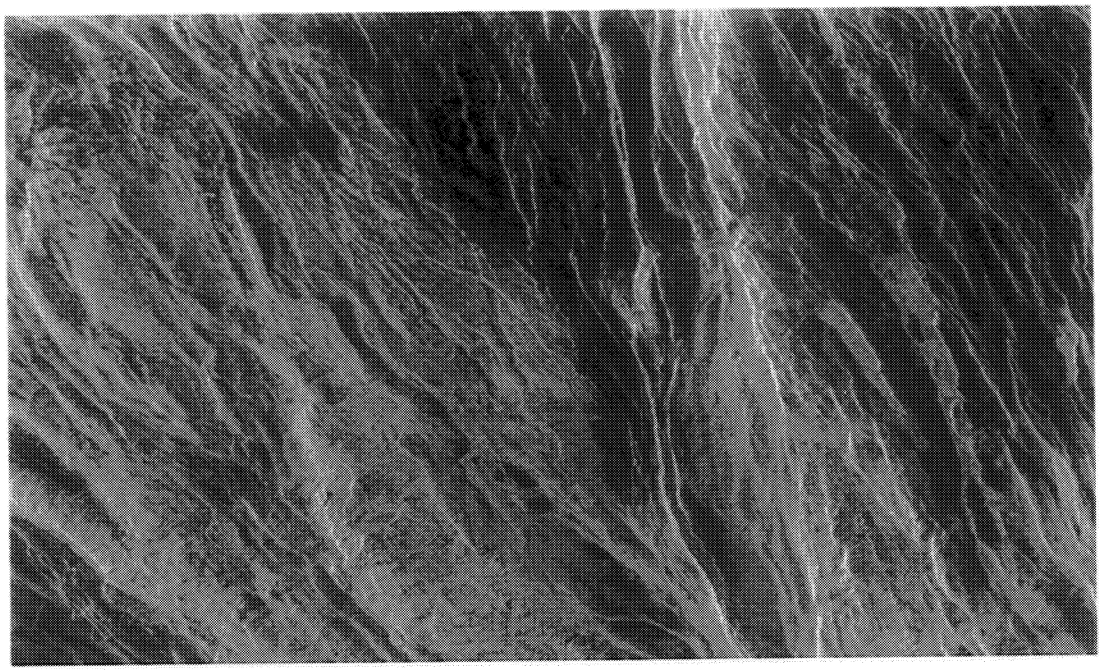

(a)

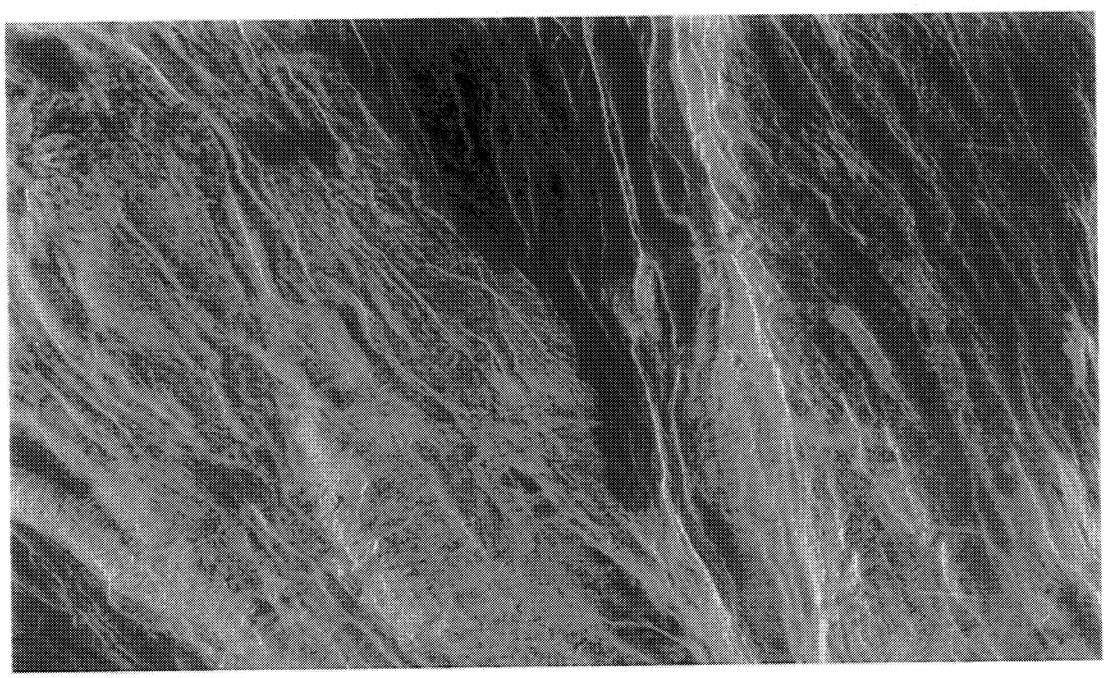

(b)

Figure 4. F–MIDR Cycle I (a) and Cycle III (b) stereo image pair; coverage is from Latitude 65.3 to 66.2 and Longitude 356.9 to 0.75. Nominal spacecraft altitude was (a) 1127 km and (b) 1115 km with look angles off nadir of about (a) 22 and (b) 33 degrees.

between the MIDR and BIDR results that is free from map projection distortions.

This area has been matched manually, including terrain breakline acquisition, giving also the opportunity to assess the performance of the automatching (for mosaics) with respect to individual operator measurements for Magellan SAR images. Later in this report we will discuss the performance of this program as used on optical photography on Earth having known accuracies.

Finally, this area has cross-polarized emissivity data, also acquired in an experimental mode. This dataset, as we shall see, can be uniquely used for roughness determination. This area is not discussed any further in this report.

3.3 Artemis Chasm, 35 South, 145 East

This area has been extensively evaluated by using stereopsis, altimetry and monoscopic methods as well as for geologic and structural content by Connors (in progress). For this reason we include this area as a study site for future work since the terrain complexity is great, offering multiple fault directions and contrasting high and low frequency terrain patterns.

For now we need to defer study of this area until further navigation corrections and other ancillary and image data become available.

4. SURFACE MEASUREMENT RESULTS

A number of DEMs were derived predominantly over the Maxwell Montes test site. Before addressing roughness determination we describe the methods and parameters used to generate these height models and present a comparison of the results.

We show results for the 3-D range-Doppler BIDR stereo solution of [Hensley and Shaffer, 1994] and that of the approximate parallax method [Leberl et. al., 1992], using a "nominal" ephemeris, for the same area and mosaic image data (MIDRs). Given the large distribution of MIDR products, it is additionally useful to assess the extent to which approximate methods produce results that differ from those obtained by intersection methods. We speculate that the accuracy of the approximate method depends on

geographic latitude, with errors increasing significantly with distance from the equator. For Maxwell the F-MIDRs have been reprocessed with ephemeris corrections so navigational errors should be minimized. In addition, for completeness and consistency we present Magellan and Pioneer Venus altimeter results.

4.1 Stereo Measurements on F-MIDRs and F-BIDRs

This section discusses the results for the test sites for which stereo processing was done, including use of stereo intersection, parallax and shape-from-shading, all applied to Maxwell Montes.

A DEM was produced using the stereo processing software developed at JPL (Figure 5a) The images strips were matched at intervals of 4 pixels and the DEM was gridded to 1 pixel [Hensley and Shaffer, 1994]. The DEM was subsequently averaged to compare with 2-pixel DEMs generated from parallax stereo. The averaging was done to decrease the noise in the DEMs.[1]

Figure 5b shows a DEM of the same area produced from the MIDRs (using about thirty-five thousand match points) using software that is part of the Magellan Stereo Toolkit [Vexcel Corp., 1994]. It uses the nominal ephemeris and approximate parallax schemes described in [Leberl, et. al., 1992]. Matching was at every 6 pixels while gridding was at 4 pixels; the DEM was supersampled using bilinear interpolation to match the resolution of the DEM from F-BIDRs. It should be noted that the MIDR DEM is thus somewhat "smoothed" while the BIDR DEM is somewhat "noisy". These are properties of primarily the match and grid spacings used.

Both DEMs were generated using the automated matching algorithm described in [Frankot et. al., 1994]. The matching software exists in two formats, one for conventional raster images (such as MIDRs) and one specialized for Magellan BIDRs. The accuracies and characteristics of the matching methods are discussed later in this report.

Figure 6 shows a series of profiles through the detailed area for the parallax and 3-D intersection DEMs. The profiles are indicated in the images of Figure 12 by the black tick marks at the left edge of the Cycle III image. Wire-mesh perspectives are shown in

[1] This work was done partly at Vexcel Corporation under the current contract.

Figure 7 for the two DEMs and Figure 8 shows IHS images with color encoded as height. Figure 9 illustrates a perspective view of the DEMs with the Cycle 3 image overlaid. Figures 10-12 show more presentations of the results including SfS DEM contours over the Cycle III image.

Table 1 lists statistics for the two DEMs. While large errors due to ephemeris have been corrected by the reprocessing of the MIDRs used in the parallax computations, the large discrepancy in the height values we believe is due to coordinate system projection errors as well as noise in the BIDR DEM. The mean difference between the MIDR and BIDR DEM after registration was ***759m + - 457m.*** The minimum and maximum differences were -2288 and 2244 respectively. The MIDR-based version relies on a simple "counting" formula for image pixel location as opposed to the BIDR version which, for each image framelet pixel, goes through exact coordinate transformation during processing.

Table 1. DEM Statistics for Maxwell Montes

	Resolution (m)	min	max	mean	stand. dev
BIDR	75	4884	10732	8155	1016
MIDR	300	5272	10081	7747	759
MGAlt	4.5k	4687	9563	7614	821
PVAlt	10k	5270	9445	7437	731
SfsMIDR	150	5228	10043	7747	759

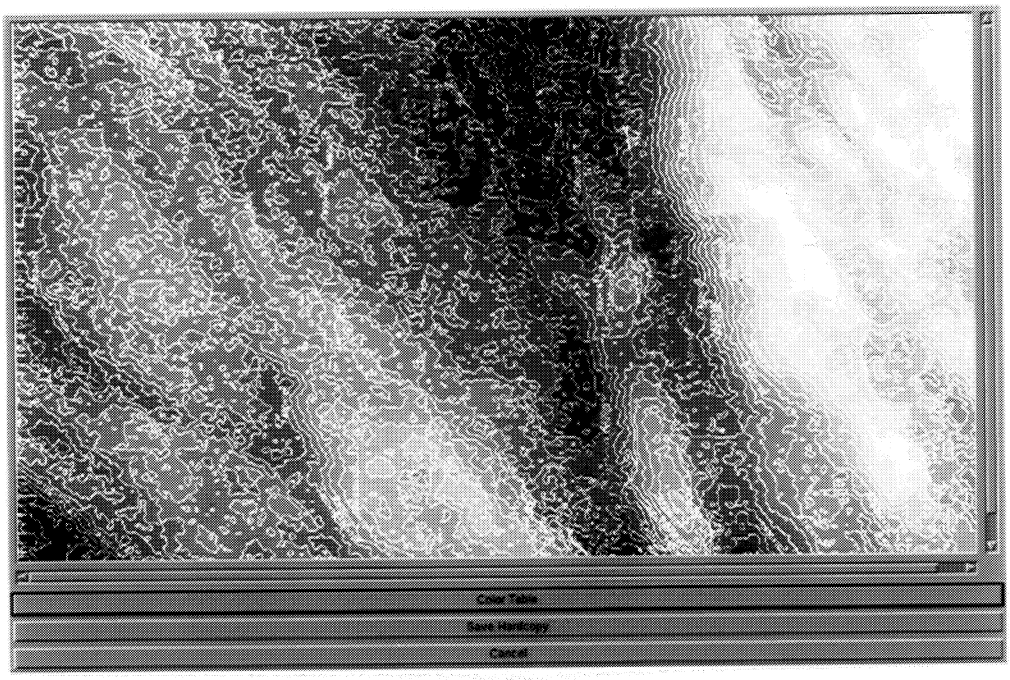

(a)

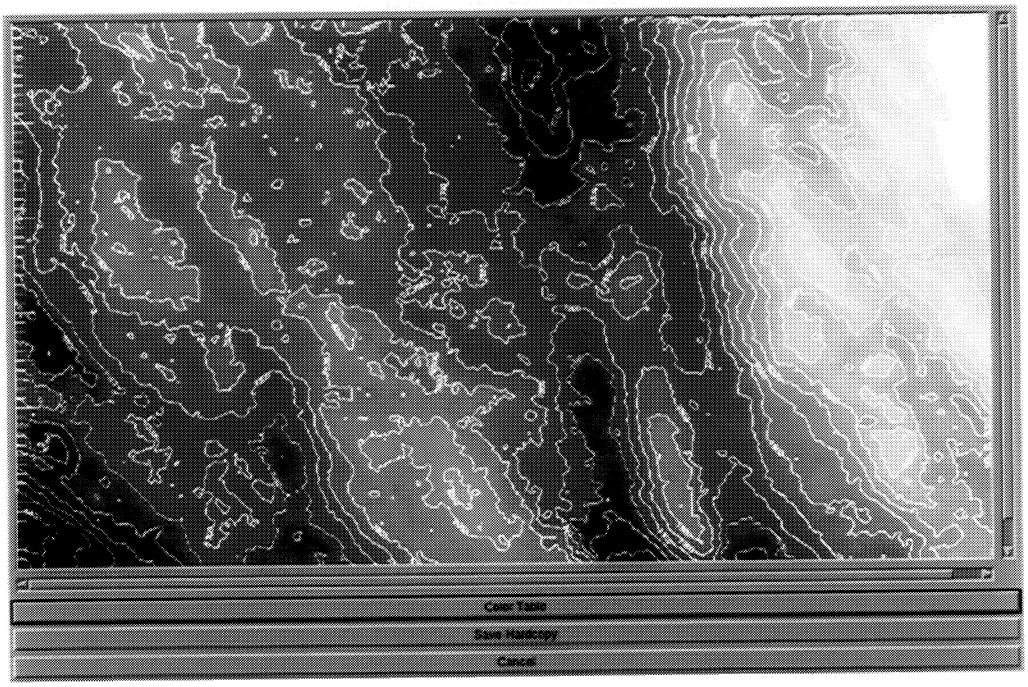

(b)

Figure 5. DEMs from F–BIDR (a) and F–MIDR (b) stereo, presented as images with contour overlay at 250 meters. The area is about Lat 65.3,66.2, Long 356.9,0.8.

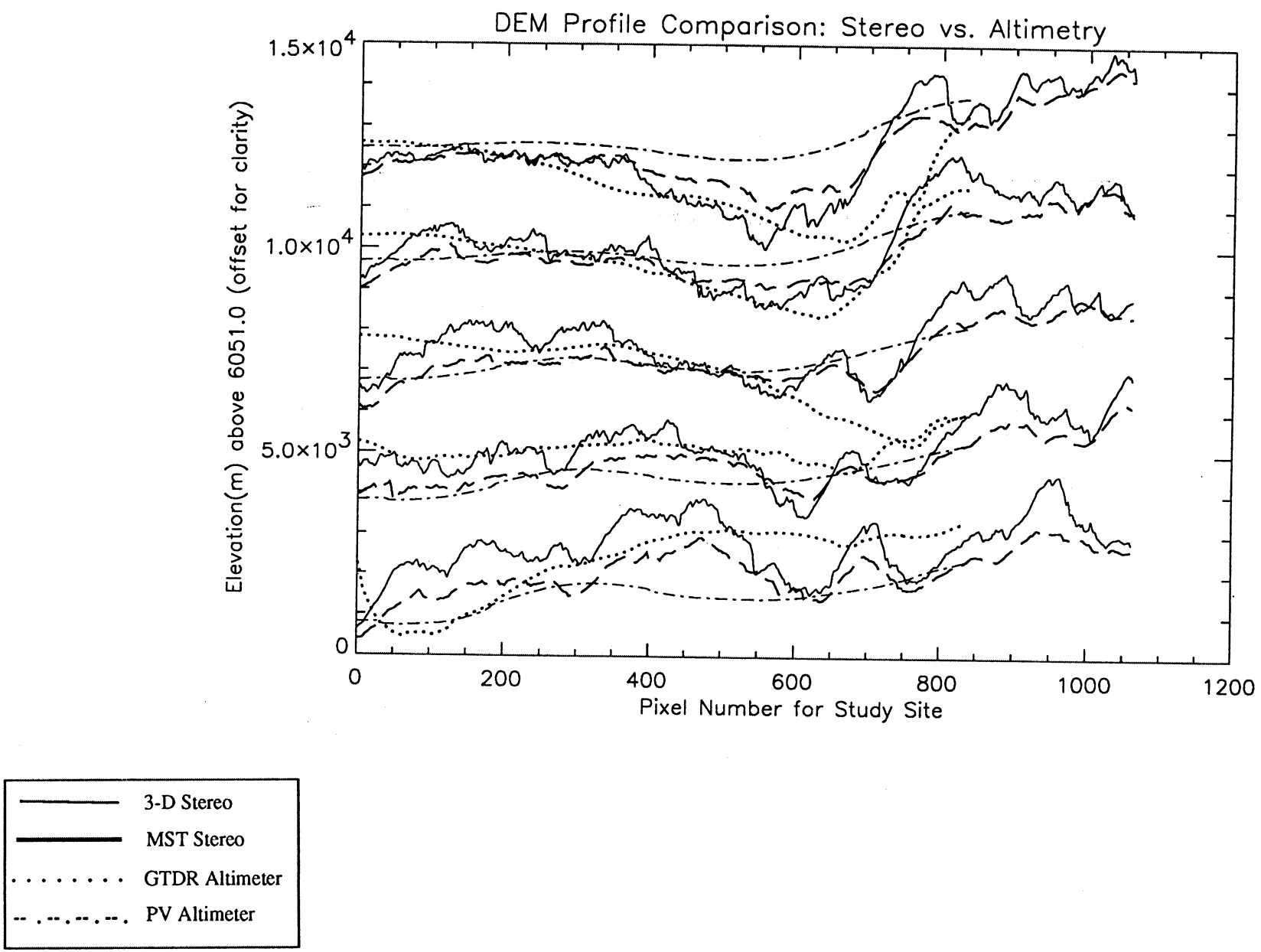

Figure 6.Elevation Profiles of the Maxwell Montes Test Site Using Different DEMs.

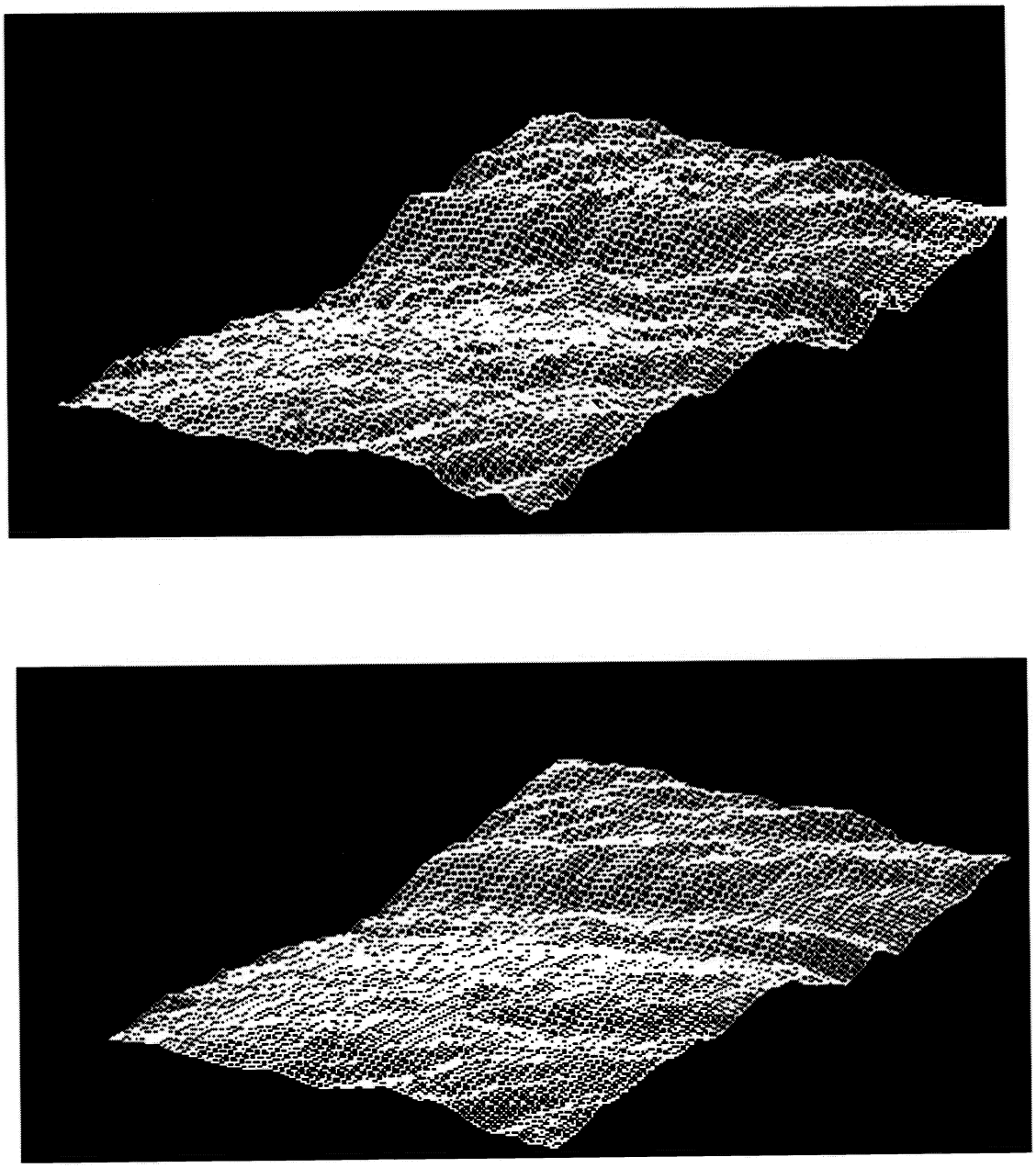

Figure 7. Wire–mesh perspectives from the Southwest for (a) the F–BIDR DEM and (b) the F–MIDR DEM. Vertical exaggeration is 20.

Figure 8a. IHS (Intensity–Hue–Saturation) presentation of the F–BIDR DEM. Height is encoded as color, intensity is the Cycle III ortho–image from F–MIDRs and saturation is a constant 40%. The color cycle wraps every 5000 meters.

Figure 8b. IHS image using the F–MIDR DEM as color and intensity and saturation as in Figure 8a.

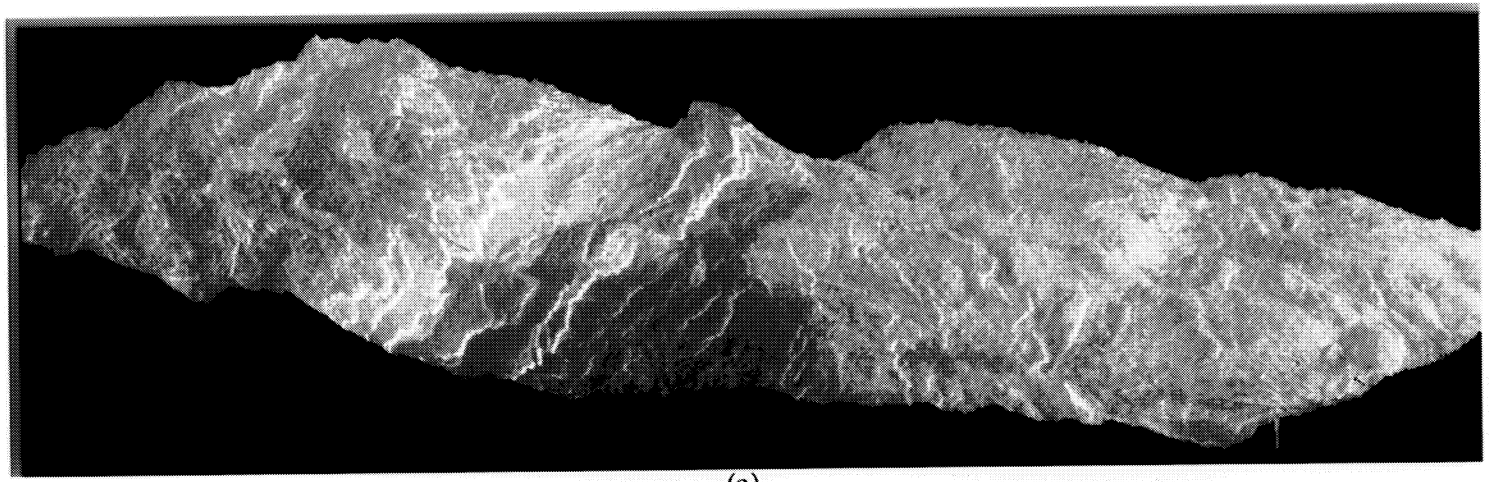

(a)

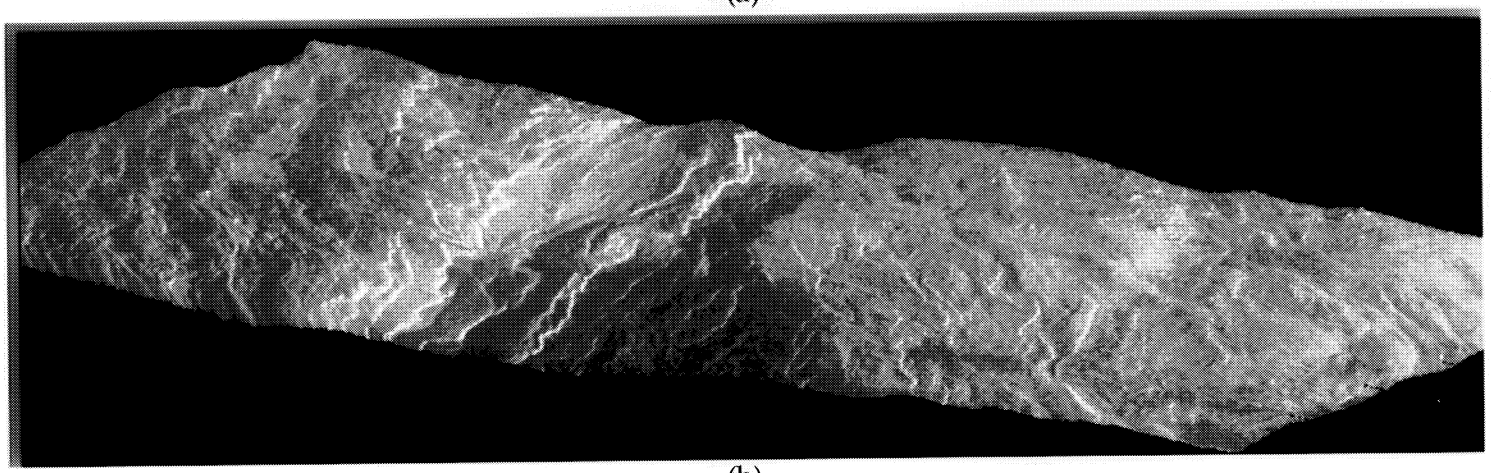

(b)

Figure 9. Perspective views of (a) F–BIDR DEM and (b) F–MIDR DEM. Vertical exaggeration is 2 with elevation angle 15 degrees, azimuth rotation –150 degrees. The Cycle III F–MIDR ortho from parallax stereo was used in draping.

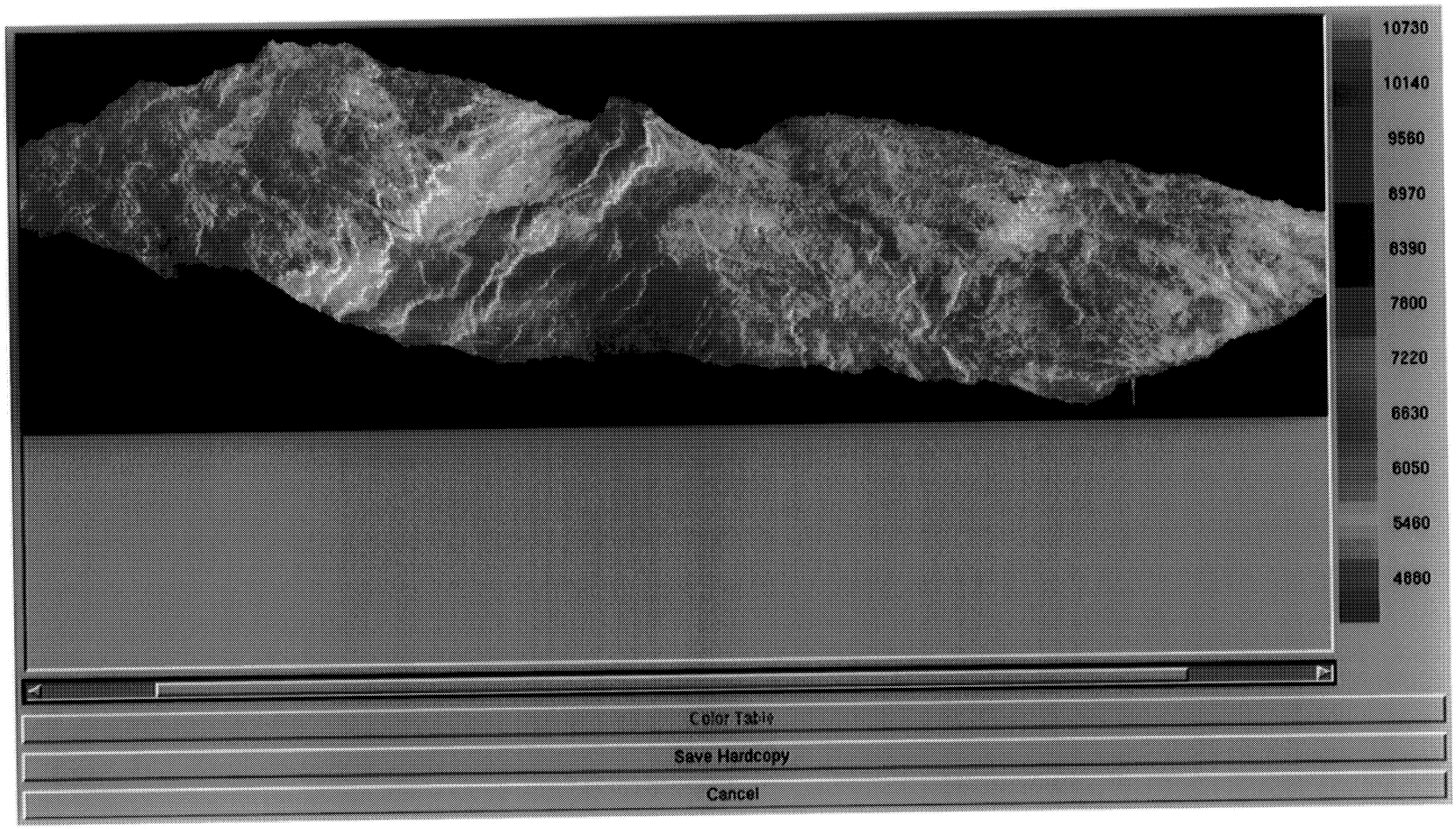

Figure 10a. Perspective of F–BIDR DEM as in Figure 9a but color encoded with the IHS image of Figure 8a.

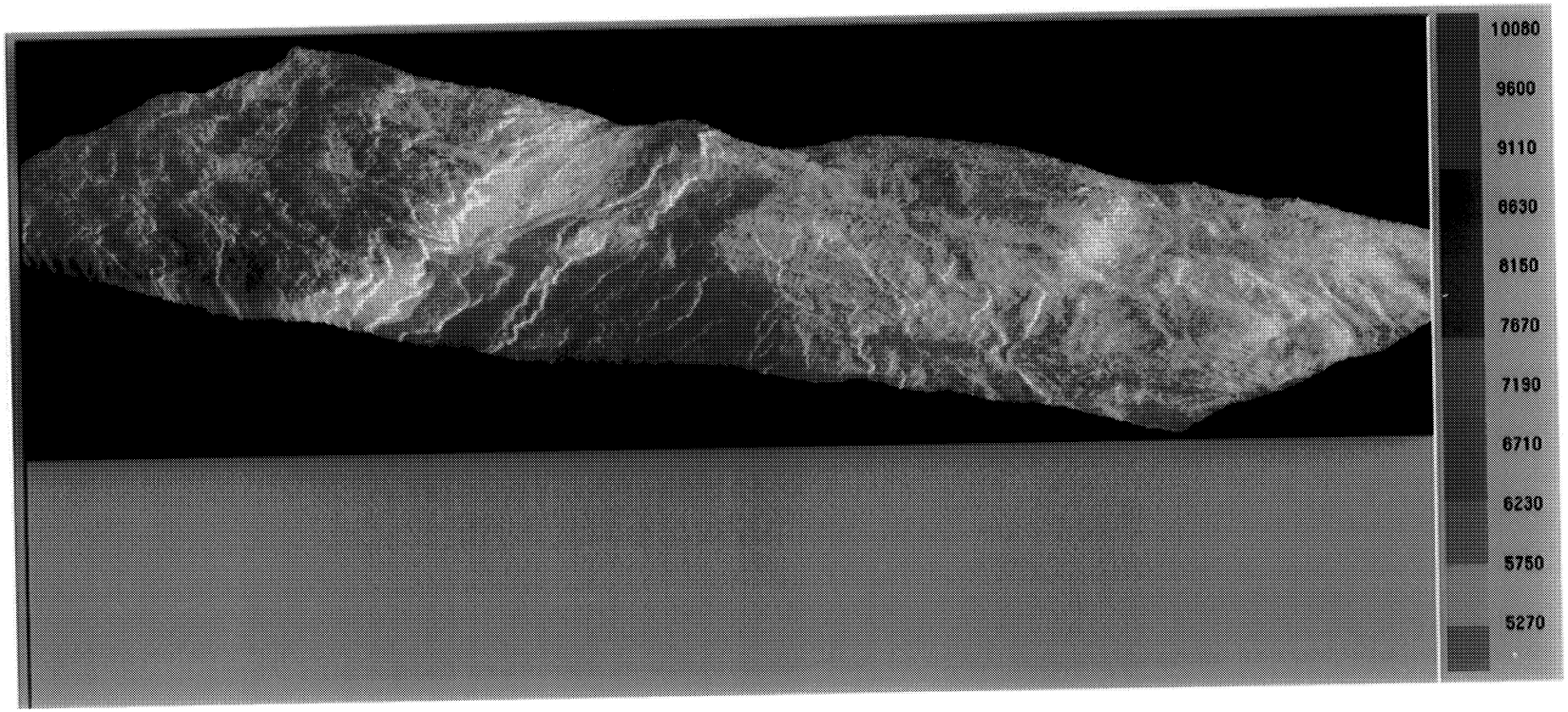

Figure 10b. Perspective of F–MIDR DEM as in Figure 9b. but using the IHS image of Figure 8b.

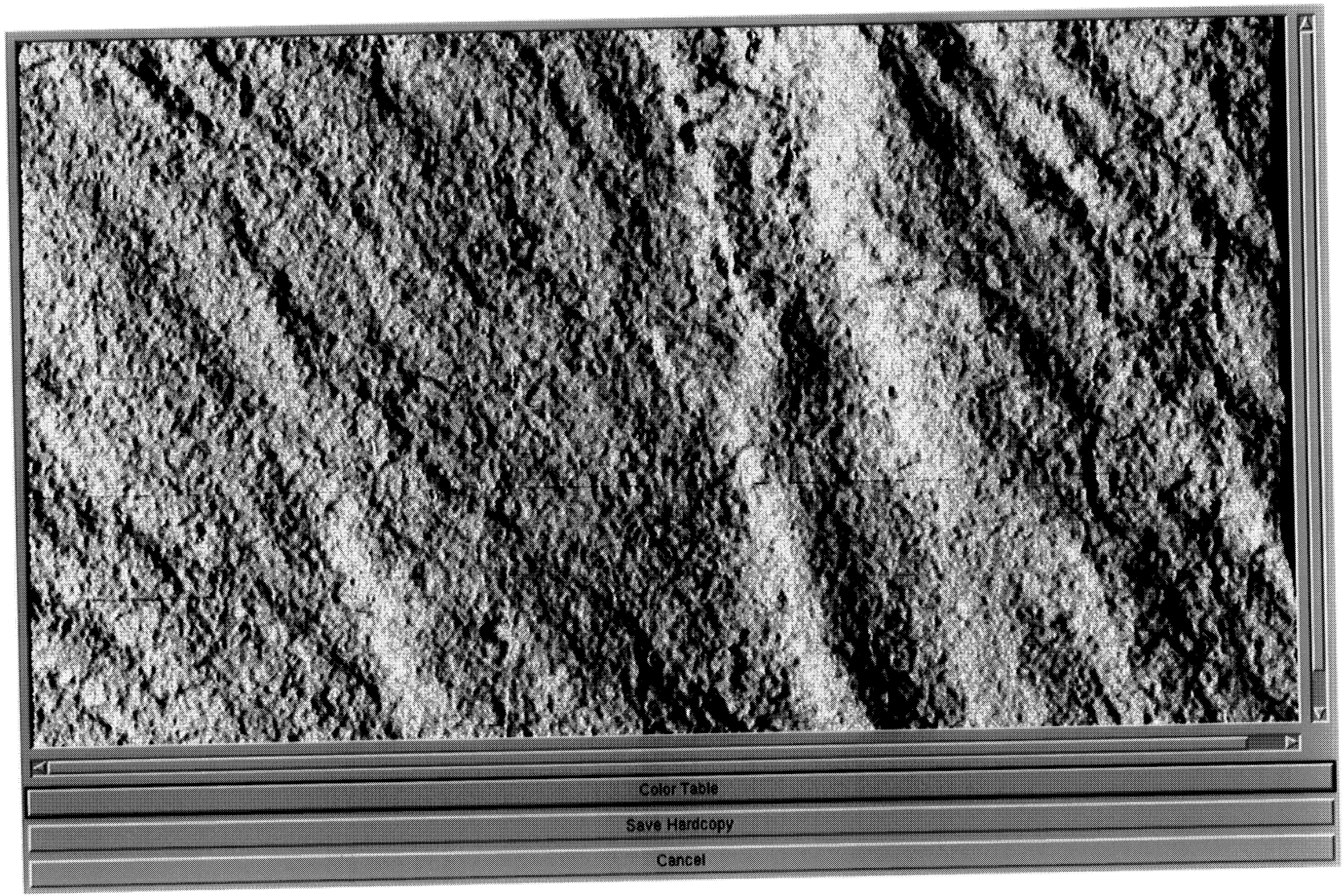

Figure 11a. Product–level simulation (non–coherent) of the F–BIDR DEM using nominal ephemeris from the F–MIDR Cycle III data and 16 looks of speckle noise.

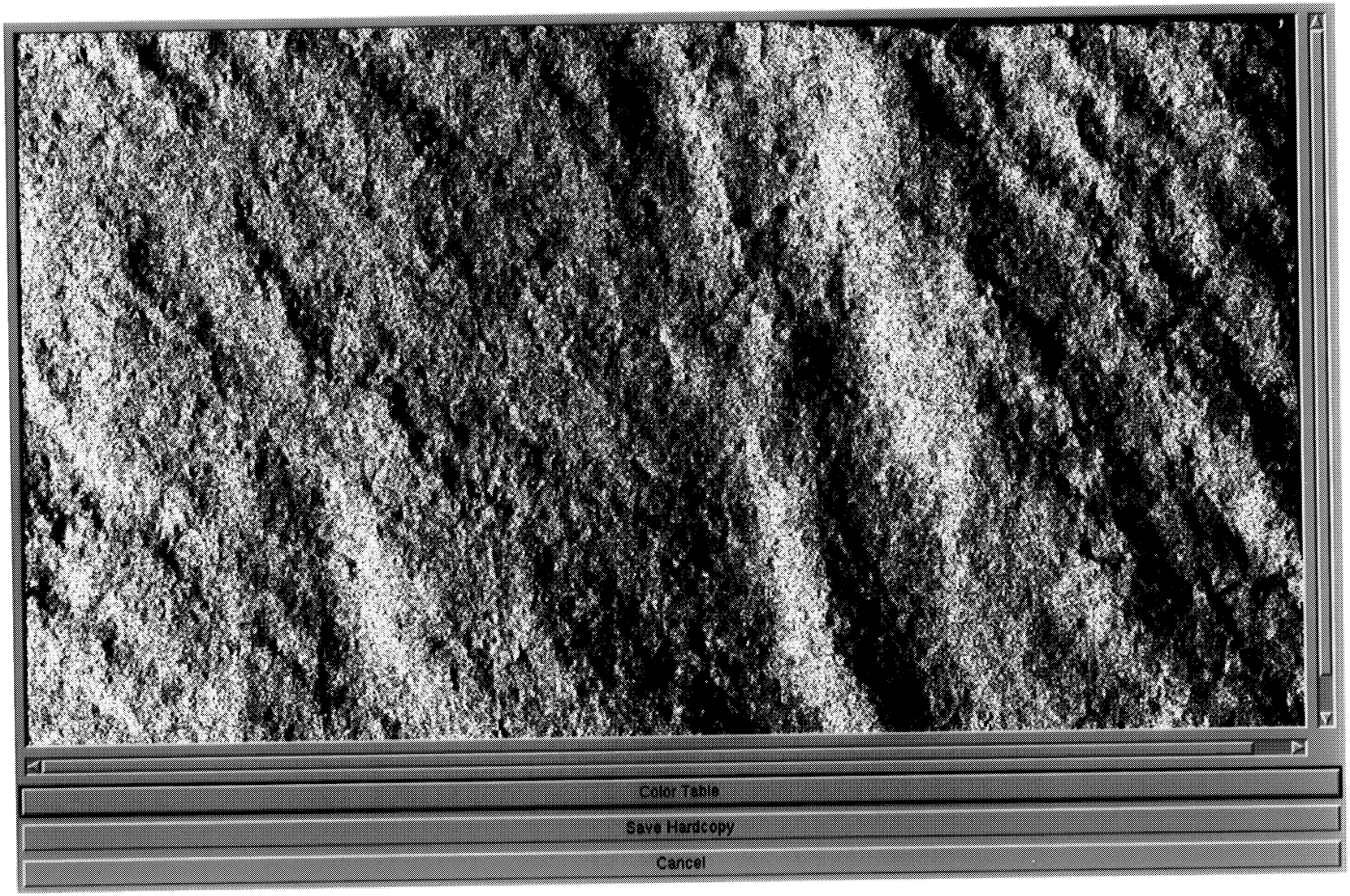

Figure 11b. Simulation of F–MIDR DEM as in Figure 11a.

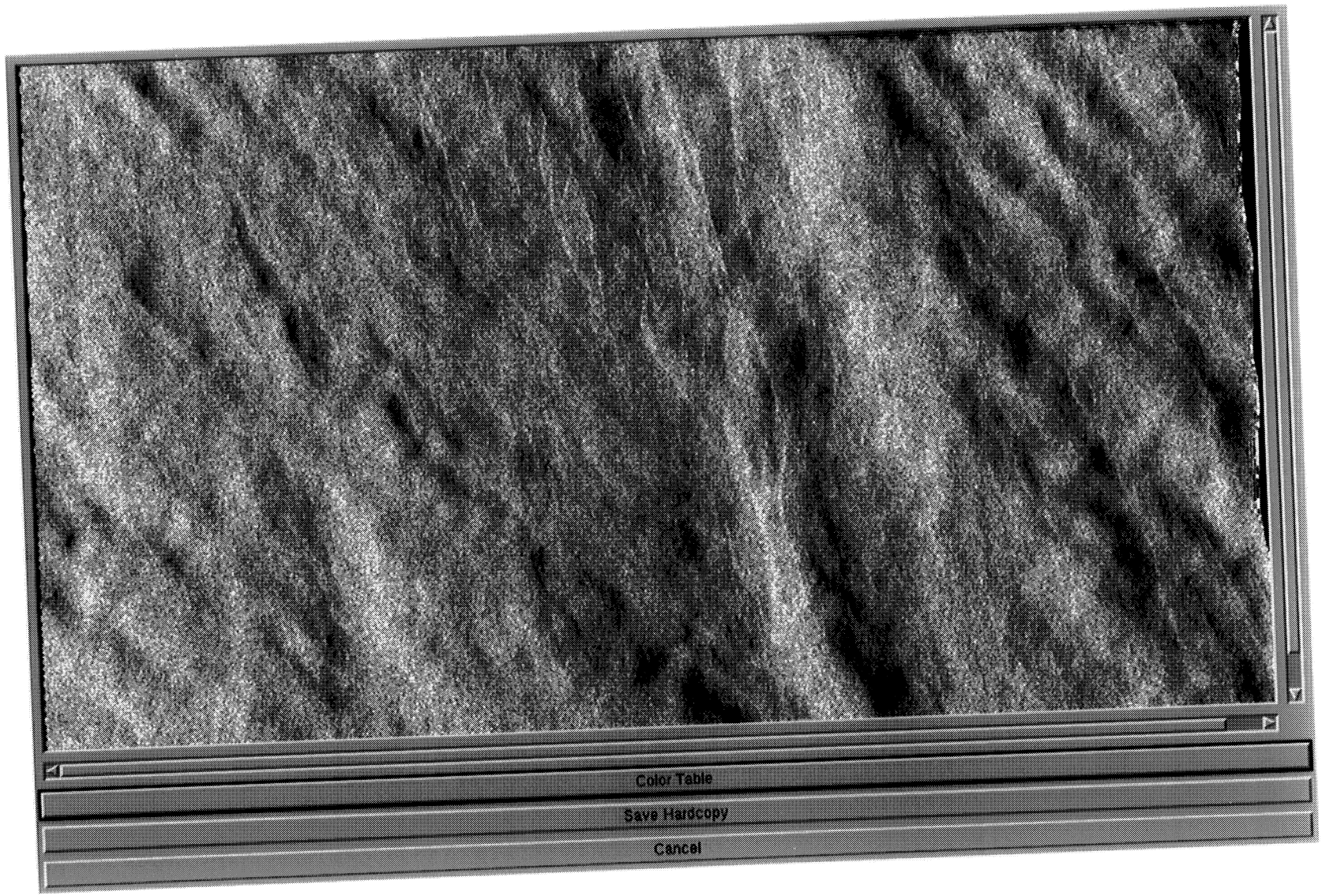

Figure 11c. Simulation as in Figures 11a,b of Shape–from–shading refined DEM from F–MIDRs. SFS iterations used was 10.

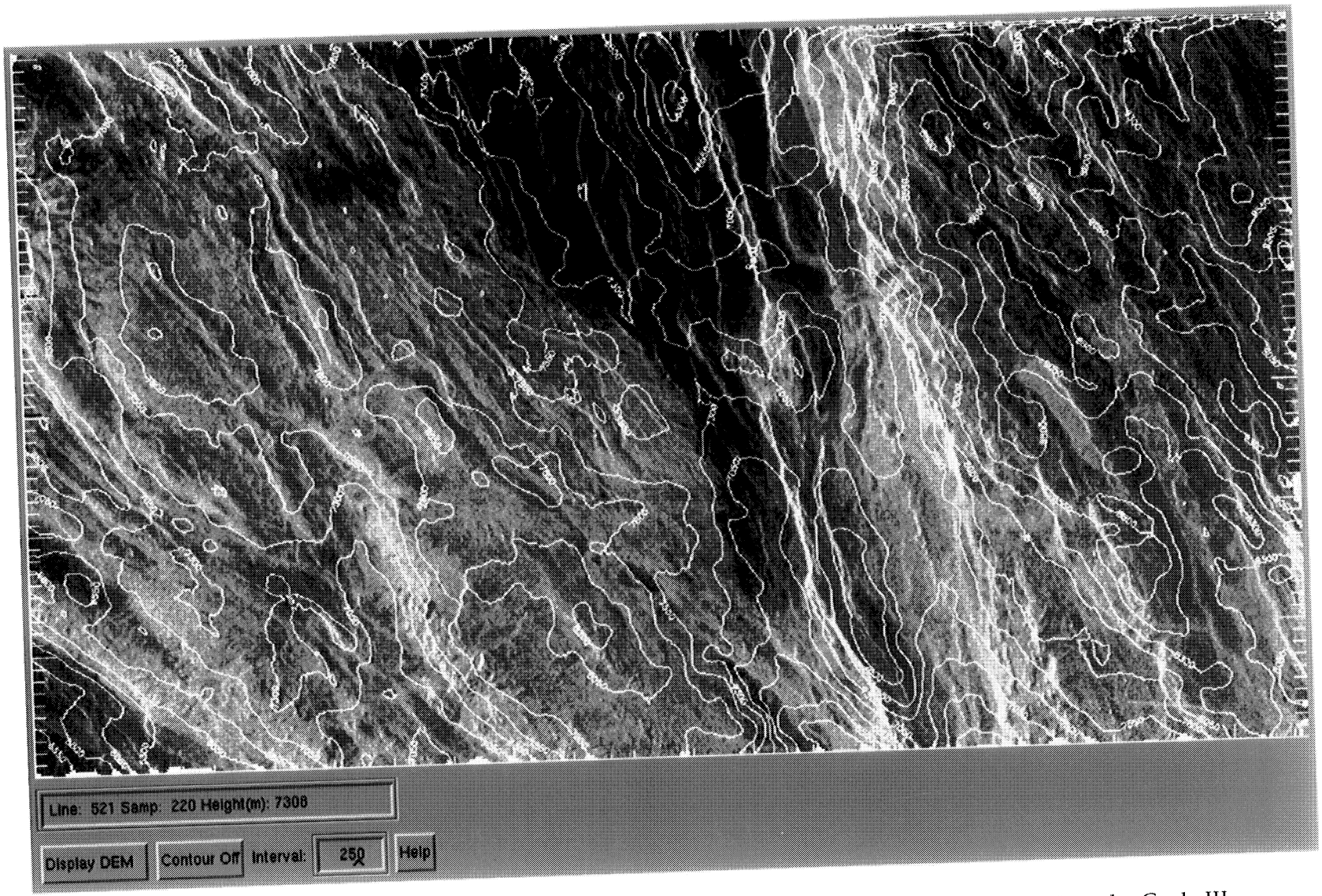

Figure 12. Image map showing 250m contours from the SFS–refined F–MIDR DEM overlaid on the Cycle III F–MIDR ortho image.

4.2 Stereo versus Altimetry

GTDR and PV Altimetry were obtained for this area (Figure 6). The values were extracted using a weighted Lagrangian interpolation that enhanced the smoothness of the altimetry at the resolution of the stereo maps. MST extracted the area but it seems as if it needed to be shifted by 225 150m pixels to register to the other DEMs. Table 1 shows the elevation ranges.

4.3 Refining a Stereo DEM with Shape-from-Shading

Shape-from-Shading (SfS) was applied to the images of Figure 4 using the MIDR DEM. Radar image simulations are shown in Figure 11c for one case. Figures 11a,b illustrate a simulation of both the stereo MIDR and BIDR DEMs indicating an improvement in detail by means of SfS. Future work will try to exploit the ability of the increased resolution DEM of SFS to remove a greater amount of local incidence angle effects thus leaving a more precise backscatter dataset for use in inversion models.

An elaborate set of results has been compiled from which Figure 11c is but a small sample. However, the analysis of the results requires further work. This analysis will be presented in the final report.

4.4 Geometric Calibration of SAR Images using a DEM

The SAR imagery is being corrected for the geometric effects of topography (terrain distortions). However, also radiometric effects need to be modeled and removed. Thus the accuracy of the DEM (from stereo or other means) affects the radiometric and geometric accuracy of the resampled ortho-image mosaics [Curlander, 1991], [Bayer et. al., 1991], [Rignot et. al., 1992].

During BIDR processing the stereo DEM is deformed by regridding the irregular elevation measurements onto a regular grid of postings through interpolation. Similarly a warping field may be derived by regularizing the computed shifts in image pixels due to the terrain relief that was determined in the stereo intersection process. Both MIDR and BIDR methods must produce ortho-image products that are registered to the DEM.

The above step is referred to as "ortho-rectification", "geometric calibration", or "geocoding". Geocoding requires further that the corrected image be transformed onto a defined map projection. Sometimes the transformation of a geometrically distorted image into a map projection is referred to as "geocoding with terrain corrections". When this step is complete the location of pixels is assumed to be correct, while the backscatter values are still fundamentally based on incidence angles that assume a spherical planet shape normalized to the Pioneer Venus topo model. Thus local incidence angle must be accounted for in the correct computation of backscatter, a process that involves the simulation of the Magellan orbit as described in Section 5.

4.5 An Experiment to Assess Automated Stereo Matching

Using Non-Magellan Imagery

In order to place the performance of the automated image matching algorithm used in this study contextually within classical image matching capabilities we have selected an aerial stereo photography pair over terrain near Albuquerque, N.M. We performed an experiment that compares the MST matcher with that of an experienced stereo operator using a standard photogrammetric stereoplotter to make manual measurements. Since photogrammetric methods of stereo measurements have been extensively tested and studied and our algorithm for matching Magellan images is robust in the sense that it can be made non-sensitive to large noise it seemed a worthwhile test to show the accuracy of the automatcher in an environment which provides stable and accurate measurement control such as that of conventional aerial stereo photogrammetry.

Since the original manual measurements do not produce image coordinates, but only a DEM, we have to perform number of transformations from image pixel into fiducial space and then to actually generate a DEM from the automated match data. Results are reported in terms of differences between the DEM from manual collection versus that from automated. Thus errors in the transformation model as well as in the DEM height interpolation must be considered.

We matched photographs represented each by 7K x 7K pixels at 32 pixel spacings where each pixel was 0.25 m on the ground as determined through the film scanning process. Due to the high variance of parallax in the stereo model we used a 6-level hierarchical

matching scheme that began with blocks of image data with 256x256 pixels and ended with 32x32 blocks. A total of ~20,000 points were matched by machine.

Results (Figure 13) give a mean difference of 12m and a standard deviation of .7 m. Expressing this in terms of pixels we find a random difference of about $\pm$ 3 pixels in elevation. Due to a base-to-height ratio of 0.6, an elevation error x is caused by a matching error $\left(\frac{x}{0.6}\right)$. This leads to the conclusions that matching differs by $\pm$4 pixels. This shows that there is some systematic bias where the matcher DEM consistently underestimated the terrain. The overall detail of the DEM and the ability to follow the terrain were very reasonable. Reasons for the bias may include photogrammetric orientation errors, match errors or interpolation errors. The difference image of Figure 13c displays a trend of decreasing accuracy as slope increases in steep terrain and increasing accuracy at lower elevations. This is perhaps because the algorithm scans from left to right. An improvement might be achieved by averaging multiple direction scans to eliminate this artifact.

It is believed that through parameter adjustments, increased point density, or improved scans, we could further improve these automatcher results to within +- 1 pixel.

(a)

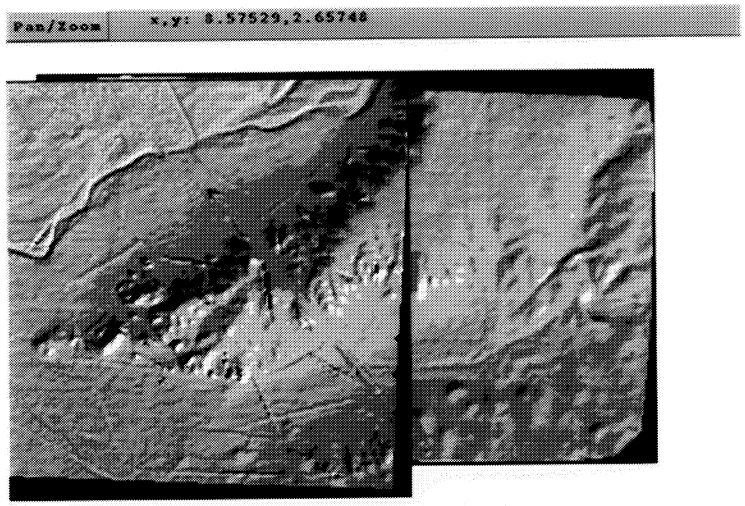

(b)

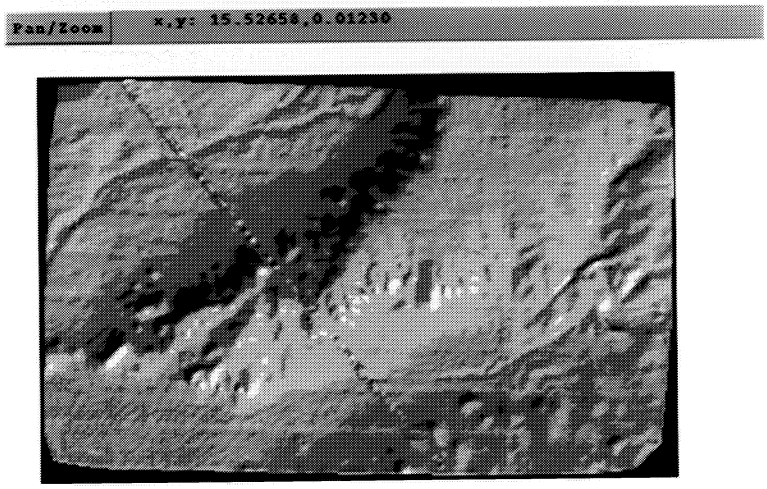

(c)

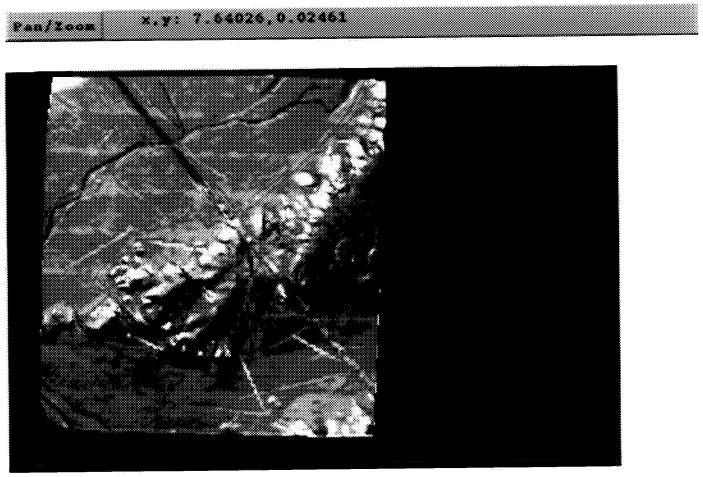

Figure 13. Results of the automatch experiment with aerial photography: (a) is a shaded relief of the DEM from manual stereoplotter measurements; (b) is the shaded relief from digital automatching; (c) is the difference DEM with grey indicating no differences.

Using Magellan Imagery

We also performed a similar experiment using a portion of the Magellan Maxwell Montes test data. In this experiment we compared DEMs (a) produced within MST from match points using the Frankot-Hensley-Shaffer algorithm; (b) produced by an algorithm developed at INRIA (National Research Institute for Information and Automation) in France. The INRIA algorithm is feature based and utilizes the epipolar geometry for match point refinement. Figure 14 presents the resultant DEMs along with contour plots and the input SAR images. No quantitative comparisons were yet made but we note here that the correspondences were reasonable at 200m levels, with more errors apparent in the INRIA algorithm probably attributable to the sparse feature-driven point sets. Future research may address the possible merging of a feature based algorithm with cross correlation in a statistics based algorithm to perhaps obtain measurements closely resembling those obtained by hand, which can model terrain breaklines.

5. REMOVING THE EFFECTS OF SLOPES FROM MAGELLAN IMAGES

Removal of slope-effects in SAR images has been studied using a number of methods. In this report we focus on removal of local incidence angle area and antenna pattern effects for Magellan images (see for example [Cheng et. al., 1994]) using stereo techniques. As an extension of this concept we are pursuing the interpolation of stereo elevation measurements using grey values (shape-from-shading) as a way to increase the resolution of the stereo topography and thus the accuracy of the roughness determination. After removal of processor area and antenna pattern local incidence angle effects we will be left with backscatter values that are functions primarily of small scale scattering and dielectric constant. Residual errors, according to [Rignot, 1992], consist of SAR processing calibration errors, as well as errors from the stereo and SfS processing.

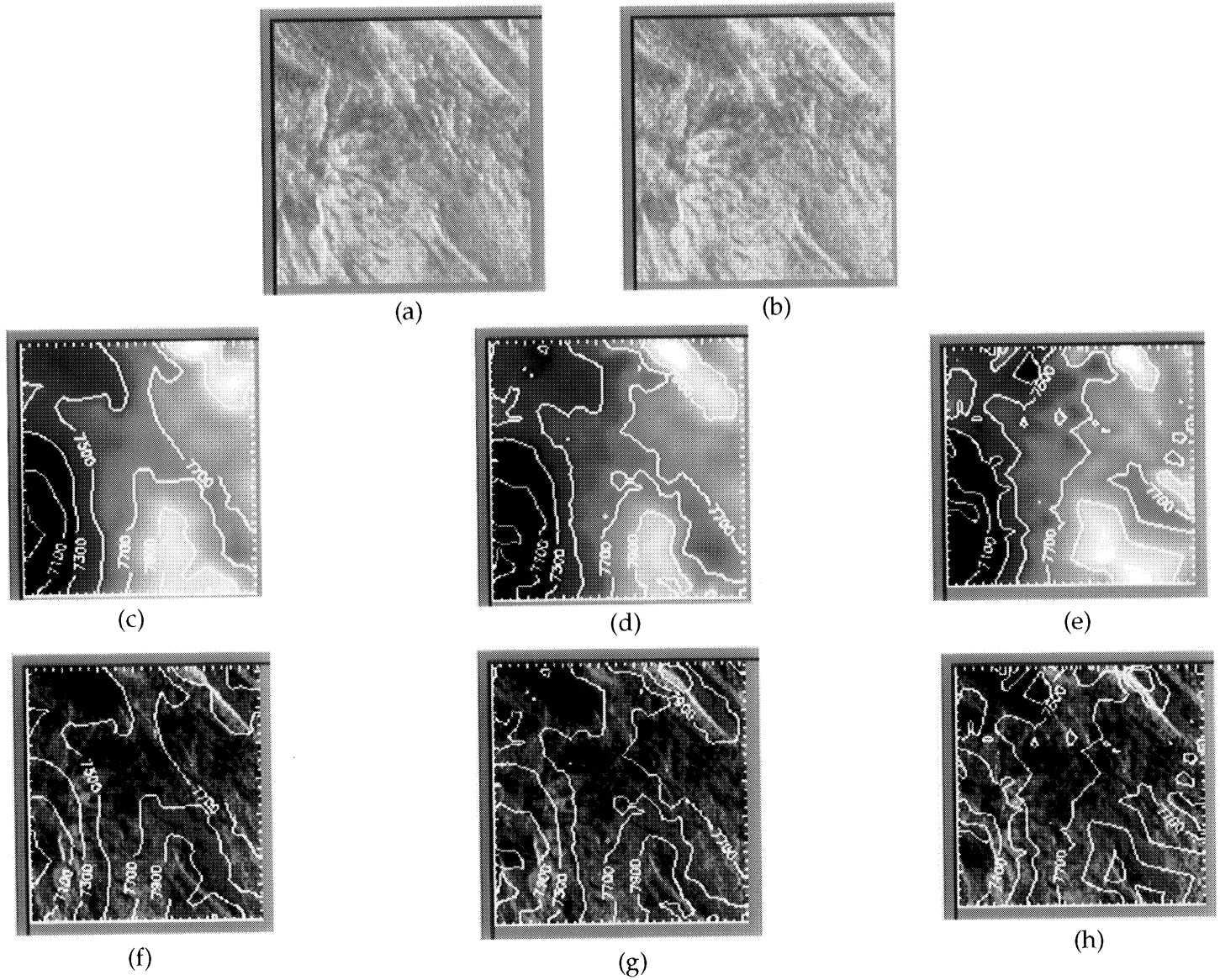

Figure 14. Comparison of Frankot–Hensley–Shaffer with NRIA Matching Algorithm: (a) and (b) are the input Cycle I, III 512x512 byte MIDR subimages; (c) and (d) are of 200m contour DEM images from Frankot–Hensley–Shaffer, with match spacing 64 and 32 pixels; (e) is the NRIA algorithm also at 200m levels; (f), (g), (h) are the contours of (c), (d), and (e) overlaid on the Cycle III SAR ortho–image.

5.1 An Approximate Computation of Backscatter from DN-Values

To some degree we can simply view or segment the resulting reduced imagery, especially over uniform cover. For Venus, and Maxwell Montes in particular, we must further remove the effects of dielectric constant to get real roughness data. The degree to which incidence angle estimation errors affect determination of dielectric constant has been studied by [Rignot, 1992]. He did show it to be significant for calibrated radar image data.

For Magellan, we can get backscatter σ_0, normalized to the Muhleman model from

$$\sigma_0 = 0.2 \text{ (pixel DN - 101) dB}$$

from which we can then correct the values directly using approximate ephemeris. A more accurate approach involves using the Magellan radiometric resampling coefficients which are in a range-Doppler coordinate system and then to actually form corrected DNs in a forward manner as described next.

5.2 A Rigorous Algorithm to Compute Backscatter from DN-Values and Terrain Slope

To reduce the geometrically corrected image mosaics we need to form the Magellan orbit and, using the high resolution stereo DEM, determine the look vector to each individual DEM scattering element. From the look vector and the local slopes we can derive the local incidence angles for each DEM posting (and thus each pixel element in the mosaic) which in turn determines the various radiometric corrections to apply to the mosaic grey values. In order to form the look angles the nearest bursts and their parameters must be located and accessed with respect to the pixels (scatterers) in the image mosaic.

In order to apply radiometric corrections using actual incidence angles due to terrain we must first remove the radiometric compensation factor applied during processing of each burst. This factor, $C_{rg}(r,f)$, is a function of r, range coordinate, and f, Doppler frequency. $C_{rg}(r,f)$ is defined as:

$$C_{rg}(r,f) = \frac{(4\pi)^3 N_r^2 N_a R^4(r,f)}{P_T(t) K N_p G_B A Q G_A^2(\theta_e,\theta_h) C_r C_d G_r(t) \lambda^2 f(I) G_{state}}$$

where

$R(r,f)$ = slant range to pixel

$$P_T(t) = \frac{\text{transmitted power of burst}}{\text{transmitted power during calibration}}$$

N_r = range FFT length

N_a = azimuth FFT length

N_p = # pulses in burst

K = transmitted power during calibration * sensor gain * processor gain

$G_A(\theta_e, \theta_h)$ = 2-way antenna pattern function, including loss through cable connecting sensor and antenna

G_{BAQ} = residual gain factor left out of the BAQ reconstruction process:

$$G_{BAQ} = \frac{1.73\ S_2}{127.0}$$

where S_2 is a function of the threshhold (a constant per burst)

G_{state} = gain for non-standard redundancy configurations

θ_e, θ_h = elevation and horizontal angles off-boresight

C_r = conversion factor from time to ground range

$$C_r = \frac{c}{2\sin(I_m)}$$

where I_m is the MRP (mid-range point) incidence angle

C_d = conversion factor from Doppler to along-track distance:

$$C_d = Rm\left(\frac{1}{2|\mathbf{V_S}|\sqrt{1-(<\boldsymbol{V_S}\ ,\boldsymbol{P}\ >)2}}\right.$$

where $\mathbf{V_S}$ = spacecraft velocity, $\mathbf{P}$ = boresight pointing vector, and $\boldsymbol{V_S}$ and $\boldsymbol{P}$ are the corresponding unit vectors

$$G_r(t) = \frac{\text{receiver gain of burst}}{\text{receiver gain during calibration}}$$

λ = radar wavelength

I = incidence angle assuming a spherical surface

$$f(I) = \frac{0.0118\cos(I)}{(\sin(I)+.111\cos(I))^3}$$

Note that the incidence angle I figures into $C_{rg}(r,f)$. In practice, a constant value I_m is used per burst where I_m is the incidence angle at MRP (the mid-range point) assuming a spherical surface. Furthermore, C_{rg} is only computed at nine points per burst and a set of quadratic equations are derived to approximate C_{rg}. These equations are of the form:

$$C_{rg}(r,f) = a(r) + b(r)f + c(r)^2$$

where

$$a(r) = a_1 + a_2\, r + a_3\, r^2$$
$$b(r) = b_1 + b_2\, r + b_3\, r^2$$
$$c(r) = c_1 + c_2\, r + c_3\, r^2.$$

Thus to remove the radiometric compensation factors applied during processing, we must do the following:

(1) Compute r (range) and f (Doppler frequency) of the selected pixel in the BIDR ortho

(2) Compute $C_{rg}(r,f)$ using $a(r) + b(r)f + c(r)\, f^2$

and

$$a(r) = a_1 + a_2\, r + a_3\, r^2$$
$$b(r) = b_1 + b_2\, r + b_3\, r^2$$
$$c(r) = c_1 + c_2\, r + c_3\, r^2$$

where the coefficients a_1, a_2, etc. are those used to radiometrically compensate the current burst.

(3) Remove $C_{rg}(r,f)$ from σ_n (normalized backscatter) to get $|X(r,f)|^2 = \frac{\sigma_n}{C_{rg}(r,f)}$ where $|X(r,f)|$ is the pixel value after range and azimuth compression.

Now we want to apply the correct value of $C_{rg}(r,f)$ to the pixel value $|X(r,f)|$ to get the new normalized backscatter σ_n.

(4) Compute the actual $C_{rg}(r,f)$ using

$$\frac{(4\pi)^3 \mathbf{N_r}^2\, \mathbf{N_a} R^4(r,f)}{\mathbf{P_T(t) K N_p G B A Q} G_A^2(\theta_e,\theta_h) \mathbf{C_r C_d G_r(t)} \lambda^2 f(I) \mathbf{G_{state}}}$$

and the actual terrain (and thereby the actual incidence angle I). Highlighted terms are assumed to be constant over the burst. Details concerning this computation follow:

(4a) To find θ_e, θ_h, and I we need to find the spacecraft position $\mathbf{X_S(t)}$, velocity $\mathbf{V_S(t)}$, and boresight pointing vector $\mathbf{P(t)}$

(4b) Given $\mathbf{X_S}$, $\mathbf{V_S}$, $\mathbf{P}$, compute C_d

(4c) Given $\mathbf{X_S}$, r, and f, intersect the range-sphere and Doppler cone with the actual Venus surface model (iteratively)

(4d) Once the intersection of the surface, range sphere, and Doppler cone is found, we can compute θ_e and θ_h and then find $G_A(\theta_e, \theta_h)$

(4e) We must also compute I:

(i) Form the vector from $\mathbf{X_S}$ to the surface intersection point $\mathbf{P_t}$ (position of target) and convert to a unit vector (see Figure 15).

(ii) Find the slope of the surface in the direction parallel to a plane containing $\mathbf{X_S}$ and $\mathbf{P_t}$

We have $\frac{de}{dy}$ and $\frac{de}{dx}$ of the surface at or near $\mathbf{P_t}$ using the DEM, where y is N/S dimension and x is E/W. The normal to the surface is found by taking the cross-product of $\frac{de}{dy}$ and $\frac{de}{dx}$.

(iii) Compute the normal to the plane containing $\mathbf{X_S}$ and $\mathbf{P_t}$

(iv) Project the surface normal onto the normal found in (iii)

(v) Subtract the projection from the surface normal

(vi) Compute I as follows:

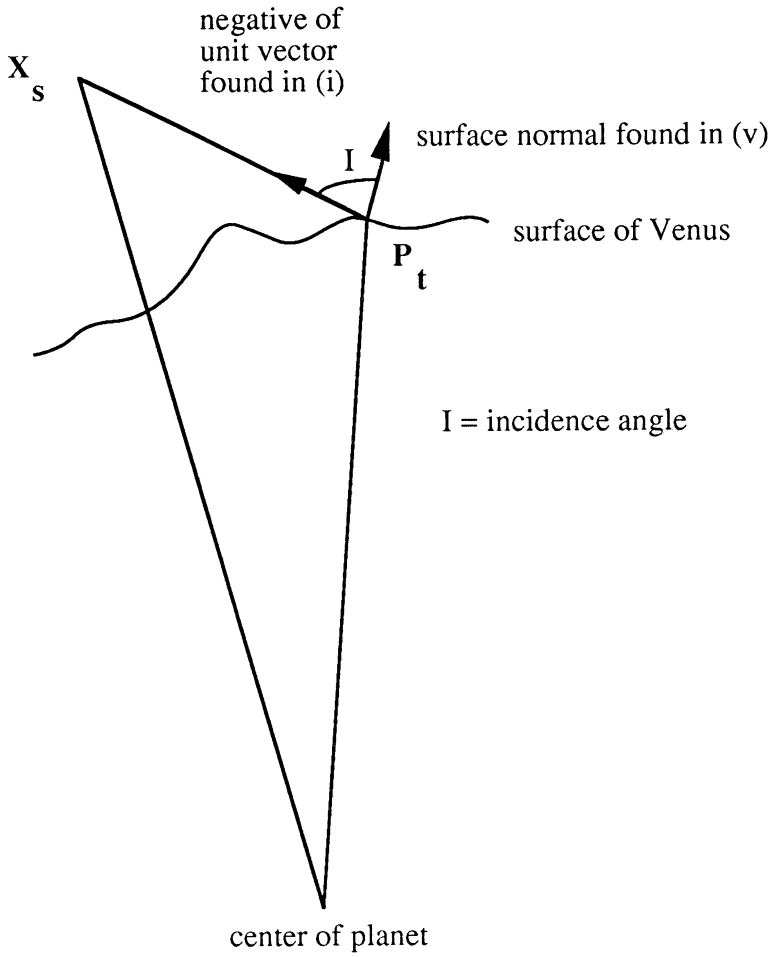

Figure 15. Definitions Used in Radiometric Corrections

a) Negate the unit vector from the sensor so it faces away from it

b) Compute dot product between the surface normal and unit vector to get I

(vii) Now find f(I).

(5) Now that we have $G_A(\theta_e, \theta_h)$, C_d, and f(I), compute $C_{rg}(r,f)$ using equation in (4) and apply to $\sigma_n = |X(r,f)|^2 C_{rg}(r,f)$.

As a result, we now have computed a new image in which each pixel is represented with its backscatter value clear of the effects of terrain slope as derived from the DEM.

5.3 Implementation Status

The program for radiometrically correcting geometrically calibrated mosaics for errors due to local incidence angle (and therefore slope) is currently being developed. This program represents the fifth element in Figure 1 which shows the F-BIDR processing parameter data and geometric mosaics as inputs and the radiometrically and geometrically calibrated image mosaics as output. Vexcel has implemented similar programs for the ERS-1, JPL Airsar and SIR-C SAR datasets and plans to utilize these code segments in finishing this program module. Other elements of this program include the Magellan orbit simulation as described above, and the access and manipulation of the processing parameter files, much of which is contained in the BIDR stereo processor.

6. MEASURING ROUGHNESS USING A DEM

A height model can be used directly to assess surface roughness at various scales. Statistics such as RMS height are only somewhat useful in that they do not provide information on the relative scales of roughness that may exist [Farr et. al., 1994]. Instead investigators have adopted a number of theories for describing the scale and degree of roughness for natural terrain surfaces.

6.1 Methods of Roughness Characterization

In particular we are interested in models for diffuse scattering which is primarily what the Magellan SAR at off-nadir look angles of up to 40 degrees will represent. Diffuse models (Bragg scattering) assume that small scale roughness (smaller than the wavelength, ie. cm to m scale) scatters the incident electromagnetic energy in a non-specular manner.

(a) Raleigh based roughness is measured by means of a root mean square change in surface elevation, σ_h.

As an indication of roughness for Magellan we can examine the Rayleigh roughness criteria (in centimeters) according to the Magellan wavelength of 12.6 cm:

smooth:: $$\sigma_h < \frac{\lambda}{25\cos\theta} = \frac{1}{2\cos\theta} \text{ cm}$$

rough: $$\sigma_h > \frac{\lambda}{4.4\cos\theta} = \frac{2.8}{\cos\theta} \text{ cm}$$

where σ_h is the root mean square variation in surface elevation.

(b) Using correlation length, RMS height determination for a given scale is possible through methods as described in [Ulaby et. al., 1986].

(c) Alternatively spectral techniques that use a log-log plot of the power spectral density of a profile of elevation data file vs. the wave number [Evans et. al., 1992], [Brown, 1987], [Farr, 1992] followed by a linear fit to determine slope and offset offer a way to generate data at different roughness scales. This method assumes that the power spectral density (PSD), denoted by G(k) of all natural terrain surfaces obey the empirical relation

$$G(k) = C\, k^{-\alpha} \qquad (4)$$

according to [Brown, 1987] and others, where $k = \frac{2\pi}{\lambda}$ is the wave number and λ is the distance along the elevation profile. This allows the extraction of slope as a measure of relative scale (steep is small cm scale roughness and flat is large) along with offset which has been described qualitatively as the "roughness amplitude". The slope can be related to self-similar fractal dimension D, by $D = 2.5 - \alpha/2$ if it can be shown that $2 \leq \alpha \leq 3$, offering additional methods for analysis and use of terrain data [Brown, 1987].

An important element in this technique is related to the moments of the power spectrum. From Fourier analysis we find that the 0th moment m_0 relates to roughness as follows

$$\sigma_h = (m_0)^{1/2} = \left[\int_{\omega_0}^{\omega_N} G(\omega)\, d\omega\right]^{1/2} \qquad (5)$$

while the second moment is the variance of slopes and the fourth is the variance of curvatures [Brown and Scholz, 1985]. Detailed analysis of these moments leads to the conclusion that the fractal dimension changes with frequency and thus can be constant only over a limited range.

For detailed information on small scale roughness however, some form of

microtopographic profile is required such as in [Farr, 1992]. It has been shown [van Zyl, 1991] that the power spectra for such microtopographic models can be estimated using model inversion techniques that use calibrated backscatter values to compute roughness. The relation

$$\sigma_h = 40.0\, e^{\,offset} \qquad (6)$$

was derived empirically by [Evans, 1992], where σ_h is roughness (RMS height) and offset was derived from the power density.

For this study, the DEMs alone are inherently limited in terms of the roughness information they provide, by their resolution, typically much greater than the radar wavelength of 12.6 cm for Magellan. In order to infer small scale roughness we must resort to the use of SAR pixel grey-value and other ancillary data as described below.

(d) Roughness from slope values [Arvidson et. al., in press] defines "roughness" as an angular value using local slopes within a scattering area. This is denoted as σ_{rms} and represents a root mean square value of slope angle.

6.2 Implementation Issues

We plan to select one or more models for direct roughness information extraction for implementation under the Magellan Stereo Toolkit. Candidates include producing slope and offset images using elevation data and other readily accessible, generally applicable functions. The correct use of these functions must be the responsibility of the "knowledgeable" user.

One exciting aspect of these roughness studies is the potential for placing stereo cameras or CCD arrays on specialized landers (eg. see [Arvidson, et. al., in press]) and acquiring microtopographic profiles directly of the venusian surface for comparison with the inversion models that are discussed in the next section.

7. MEASURING ROUGHNESS USING A MAGELLAN IMAGE AND RADIOMETRY DATA

7.1 Methods of Dielectric Determination

For Magellan we have a direct means to estimate the dielectric constant by using the Magellan radiometer data. From the radiometer data, which measure emissivity, we can estimate the dielectric constant ε from the formula (see [Arvidson. et. al., in press]):

$$e_a(\theta) = 1 - \frac{1}{2}\left(\frac{\cos\theta - \sqrt{\varepsilon - \sin^2\theta}}{\cos\theta + \sqrt{\varepsilon - \sin^2\theta}}\right)^2 - \frac{1}{2}\left(\frac{\varepsilon\cos\theta - \sqrt{\varepsilon - \sin^2\theta}}{\varepsilon\cos\theta + \sqrt{\varepsilon - \sin^2\theta}}\right)^2 \qquad (7)$$

where e_a is the average emissivity which can be computed by averaging observed H and V emissivity values (for Magellan Stereo Experiment only); θ is the local incidence angle and ε is the unknown dielectric (assumed to be the real part only). Note that equation (7) simplifies to equation (1) if the incidence angle approaches 0.

Since the resolution of the radiometer data is much lower that the SAR we must assume continuity of the geologic units being measured; that is we will find aggregate pixels that are of the same chemical properties for areas that are larger than the size of the radiometer footprint.

Another method has been reported by [Rignot, 1992], for JPL Airsar images, that is independent of "roughness" (using the Small Perturbation Model)

$$\gamma = \left[\frac{\left[(\varepsilon - 1)\sin^2\theta + \varepsilon\right]\left[\cos\theta + (\varepsilon - \sin^2\theta)^{1/2}\right]^2}{\left[\varepsilon\cos(\theta) + (\varepsilon - \sin^2\theta)^{1/2}\right]^2}\right]^2 \qquad (8)$$

where γ is the ratio between calibrated SAR VV and HH backscatter values, θ is local incidence angle, and the dielectric constant is again to be solved for.

We need to find a general way to compute a pixel-by-pixel estimate of dielectric constants for Magellan data (without cross-polarized emissivity data), which we expect to be quite high for instance for the Maxwell Montes [Ford, 1994], [Tyler et. al., 1992] area.

Estimates of dielectric constant allow reduction of the grey-values to images that are then a function only of small scale roughness and calibration errors.

7.2 Methods of Roughness Determination (Model Inversion)

(a) Using the results of ground based experiments without dielectric properties

One way to convert from the qualitative reduced backscatter values to quantitative roughness indicators requires inversion of a scattering model to produce pixel-by-pixel maps of "offset" as described by (ie in equation (6)) [van Zyl, 1991], [Evans, 1992]. For instance, we can compute roughness, σ_h (RMS height), from an empirical formula by [Rignot, et. al., 1992], where σ^0_{HH} is the backscatter of a scatterer at HH-polarization:

$$\sigma_h = \frac{0.2\ \sigma^0_{HH}}{(\exp(-0.722) + \sigma^0_{HH})(k\ \sin(\theta_i)\cos^4(\theta_i))}. \qquad (9)$$

Here k is the wave number, θ_i is the incidence angle. This formula is only valid, however, for calibrated SAR data and slightly rough surfaces but does offer a method dependent only on HH backscatter values.

For Magellan there needs to be derived a form or extension for the inversion of the small model perturbation [Rice, 1951], [Kim and Rodriguez, 1992], [Ulaby, 1985] or other model that can be used to infer small scale roughness as described above.

(b) Using a Model with Specular and Diffuse Components

In [Arvidson, et. al., in press] we find the most detailed formulation to date on inversion for diffuse scattering of Magellan data. It is briefly stated below.

First we form a specular component to the scattering model as we assume a two-scale (Kirchoff and Bragg scattering) linear combination approach [Kim and Rodriguez, 1992]. We denote the quasi-specular component of backscattering as $\sigma^0_{QS(\theta)}$ where θ is incidence angle:

$$\sigma^0_{QS(\theta)} = \frac{\rho 0}{2\cos\theta} N(\theta). \qquad (10)$$

Here ρ_0 is the Fresnel power reflection coefficient at nadir, calculated as

$$\rho_0 = \left(\frac{\sqrt{\varepsilon} - 1}{\sqrt{\varepsilon} + 1}\right)^2 \qquad (11)$$

and N is the facet number density (see [Arvidson, et al., in press]). Similarly, the diffuse component is modeled as

$$\sigma_{0,D} = 2\,\rho_0\, n \cos^n\phi \qquad (12)$$

where n is a controlling exponent for weighting the backscatter according to incidence angle. When we combine the two components linearly and expand N (see [Arvidson et. al., in press]) we get the forward direction of the inversion formula for roughness σ_{rms} as a function of backscatter $\sigma 0$:

$$\sigma_0 = (1 - f_D)\,\sigma_{0,QS} + f_D\sigma_{0,D} = (1 - f_D)\frac{\rho_0 \sec^4\theta}{2\tan^2\sigma_{RMS}} \exp\left(-\frac{\tan^2\theta}{2\tan^2\sigma_{RMS}}\right) + 2\,f_D\,\rho_0\, n \cos^n\phi$$

.

(13)

We have observed backscatter $\sigma 0$, f_D is a percentage the user assumes to be diffuse; values for σ_{rms} are angular as defined in section 6.1(d).

(c) Other Methods

Other methods that are alternative to the SPM include UPM (Unified Perturbation Method [Kim and Rodriguez, 1992]) and use of solutions to the full wave equation, incorporating multiple reflections [Bahar, 1994].

While external calibration does not exist for Magellan its internal calibration effects are fairly well known and it is a good candidate for the investigation and development of inversion techniques and correlation with surficial morphology for the determination of processes and rates for deposition such as that being investigated by [Arvidson et. al., in press].

7.3 Implementation Issues

We plan to select one or more models of roughness determination for implementation under the Magellan Stereo Toolkit. Candidates include use of the two-scale inversion model of [Arvidson, et. al., in press], and other model inversions that are available for Magellan SAR data. A preliminary specification of modules is given in Figure 16

showing direct roughness determination, dielectric determination and backscatter inversion models as functions. We would like to host a suite of various methods that can be used and compared by investigators doing roughness studies.

More theoretical work must be done on appropriate models and their inversions for Magellan data where HH and VV cross-polarized emissivity data is unavailable. Figure 16 details the system specification for a roughness modeling process similar to that described in [Arvidson, et. al., in press].

8. MEASURING ROUGHNESS USING MULTIPLE MAGELLAN IMAGES AND RADIOMETRY DATA

The most interesting aspect of using multiple Magellan images for roughness determination is the aspect of SAR imaging that inherently provides information about roughness of different scales according to the look angle geometry of the radar. The task remains to find ways to combine the information from the multiple images into a single quantitative description of roughness.

Presumably the Cycle III data will have more variance after reduction [Bayer, 1991] then the Cycle I image since it has higher grazing angle but there may be areas from the steeper imaging that may be enhanced as well. Incorporation of the right-look Cycle II image would give an additional roughness image that should represent roughness at a slightly different scale than the stereo data. These represent differences in small scale roughness that are separately enhanced by the respective imaging geometries.

9. OUTLOOK AND PLANS

We plan to increase our test site coverage with more BIDR data and to finish implementation of the radiometric correction programs. This completes the

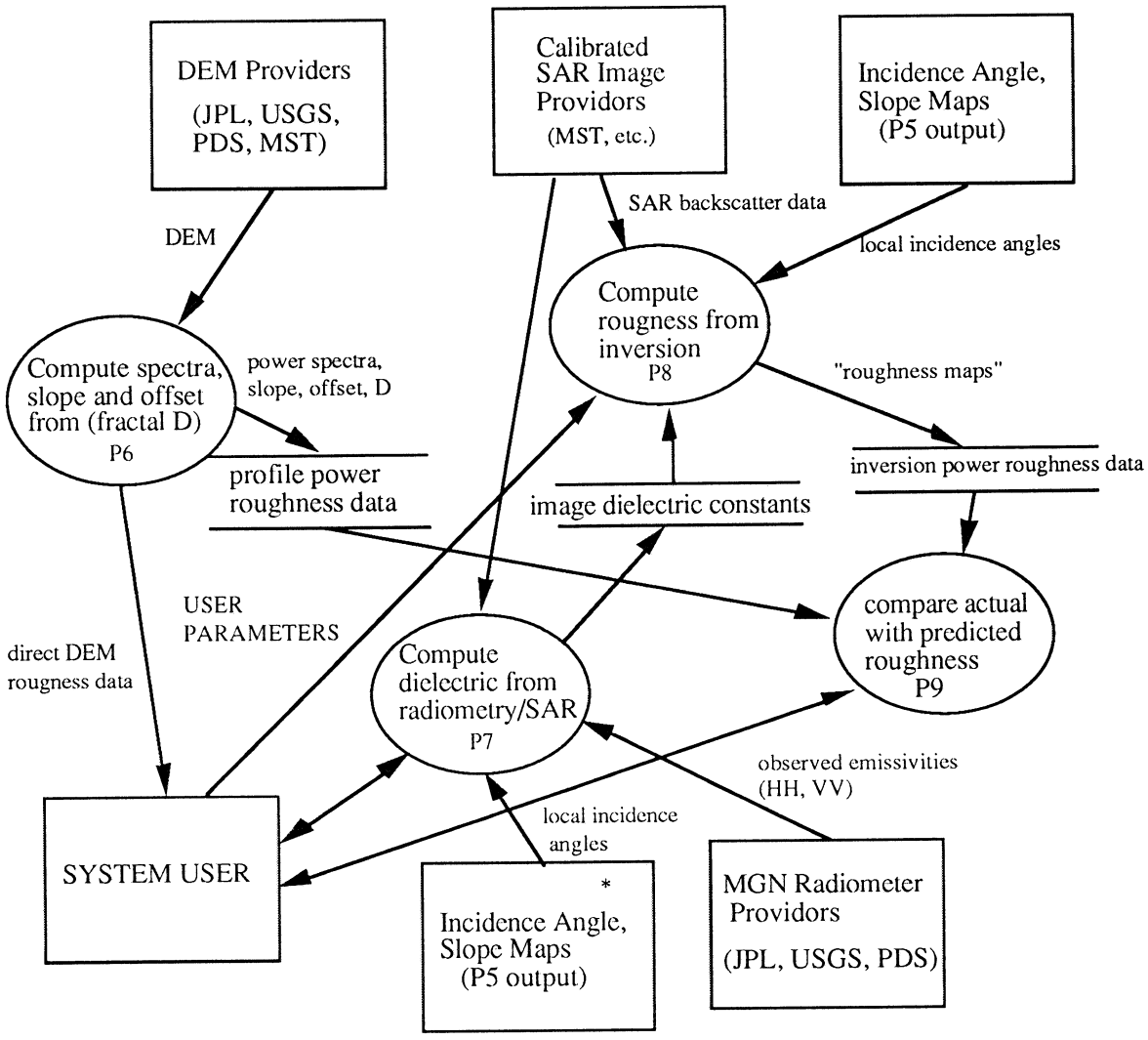

Figure 16. Data-flow diagram (DFD) for dielectric constant and roughness determination programs. Note: P1-P5 software programs are described in Figure 1.

collection of an end-to-end Unix-based BIDR stereo processing program set that can be used by Magellan investigators in their detailed surface studies. We also intend to clarify and codify availability of ephemeris corrections and supplement them with relative corrections where unavailable.

Also we will investigate, derive and if possible exercise one or more of the techniques for terrain roughness characterization including correlation, inversion and fractal modeling; in particular we will investigate an appropriate form for an inversion model for use with Magellan data.

Our estimates of roughness at various sub-wavelength scales can be input to process modeling programs that can infer rates of processes such as that done by [Arvidson, et. al., 1992].

Finally, we plan to show that increasing the DEM resolution through a rigorous stereo-constrained application of shape-from-shading to F-BIDRs produces improved radiometric correction capability of the SAR images. These new calibrated images, we hypothesize, will in turn propagate into better estimates of surface roughness and hence surface process modeling and dating.

10. REFERENCES

Alexandrov, Y.N., A.A. Crymov, et. al. (1986) Venus: Detailed mapping of Maxwell Montes region, *Science*, 231, 1271-1273.

Akima, H. (1978) A method of bivariate interpolation and smooth surface fitting for irregularly distributed data points, *ACM Trans. on Mathematical Software*, 4(2): 148-159.

Arvidson, R.E., D. Evans, et. al. (1992) Characterization of lava flow degradation in the Pisgah and Cima volcanic fields, California using remote sensing data, *Geol. Soc. Amer. Bull.*, in press.

Arvidson, R.E., M.K. Shepard, et al. (1994) Microwave signatures and surface properties of Ovda Regio and surroundings, Venus, in press.

Bahar, E. (1991) Full wave analysis for rough surface diffuse, incoherent radar cross sections with height-slope correlations included, *IEEE Trans. on Antennas and Propagation*, 39, 1293-1304.

Bayer, T., R. Winter, G. Schreier (1991) Terrain influences in SAR backscatter and attempts to their correlation, *IEEE Trans. on Geos. and Rem. Sens.*, 29, 451-462.

Brown, S.R. (1987) A note on the description of surface roughness using fractal dimension, *Geophys. Res. Letters*, 14, 1095-1098.

Brown, S.R., C.H. Scholz (1985) Broad bandwidth study of the topography of natural rock surfaces, *J. of Geophys. Res.*, 90, 12575-12582.

Cheng, T., Jin M., Curlander, J. (1994) Refinement of Magellan Radiometric Correction Using Range Centroid Estimation, *Proc. Int. Geosci. Remote Sensing Symp. (IGARSS '84)* (Strasbourg, France), 1167-1170.

Chodas, P.W., S.A. Lewicki, et al. (1993) High Precision Magellan Orbit Determination for Stereo Data, AAS/AAIA Astrodynamics Specialist Conference, August, 1993.

Davies, M.E., T.R. Colvin, et al. (1992) The rotation period, direction of the North Pole, and geodetic control network of Venus, *J. of Geophys. Res.*, 97(E8): 13141-13151.

Dohrenwend, J.C., L.D. McFadden, et al. (1984) K-Ar dating of the Cima volcanic field, eastern Mojave Desert, California: Late Cenozoic volcanic history and landscape evolution, *Geology*, 12, 163-167.

Dohrenwend, J.C., L.D. McFadden, B.D. Turrin (1987) Drainage development on basaltic lava flows, Cima volcanic field, southeast California, and Lunar Crater volcanic field, south-central Nevada, *Geol. Soc. Amer. Bull.*, 99, 405-413.

Domik, G. (1984) Evaluation of radar stereo viewability by means of a simulation technique, *Proc. Int. Geosci. Remote Sensing Symp. (IGARSS '84)* (Strasbourg, France), 643-646.

Dowman, I., C. Clark, M. Denos (1992) Three dimensional data from SAR images. ISPRS XVIIth Congress, Washington, DC, 425-427.

Evans, D., T. Farr, J.J. van Zyl (1992) Estimates of surface roughness derived from synthetic aperture radar (SAR) data, *IEEE Trans. Geosc. Rem. Sens.*, 30, 382-389.

Farr, T. et al. (1993) Radar interactions with geologic surfaces. *Guide to Magellan Image Interpretation*, JPL Publication 93-24, 45-56.

Farr, T. (1992) Microtopographic evolution of lava flows at Cima volcanic field, Mojave desert, California, *J. of Geophys. Res.*, 97, 15171-15179.

Frankot, R.T., S. Hensley, S. Shafer (1994) Noise resistant estimation techniques for SAR image registration and stereo matching, IGARSS 1994, Vol. II, 1151-1156.

Frankot, R.T., R. Chellappa (1987) Application of a shape from shading technique to synthetic aperture radar imagery, *Proc. Int'l Geoscience and Remote Sensing Symposium*, Ann Arbor, Michigan.

Hagfors, T. (1967) A study of the depolarization of lunar radar echoes, *Radio Science*, 445-465.

Hagfors, T. (1964) Backscattering from an undulating surface with applications to radar returns from the moon, *J. Geophys. Res., 69*, 3779-3784.

Hensley, S., S. Shaffer (1994) Automatic DEM generation using Magellan stereo data, IGARSS 1994, Vol. III, 1470-1472.

Hensley, S. (1992) Magellan stereo solutions and navigation sensitivities (Inter-office Memo 3346/92.002).

JPL (1990), *F-BIDR / F-TBIDR / F-SBIDR / F-XBIDR Software Interface Specification.*

JPL (1991a), *Magellan Planetary Constants and Models* (1991) 630-79 Rev. D.

JPL (1991b), *F-MIDR Software Interface Specification*

Kim, Y., E. Rodriguez (1992) Comparison of the unified perturbation method with the two-scale expansion, *Trans. on Geosc. and Rem. Sens.*, 30(3): 510-515.

Kirk, R. (1987) Thermal evolution of ganymede and implications for surface features, PhD Disstertation Thesis. Cal. Inst. Techn.

Leberl, F.W., K. Maurice (1994) Automated radar image matching experiment, *J. of Photog. and Rem. Sens.*, Vol. 49(3): 19-33.

Leberl, F.W., J. Thomas, K. Maurice (1992) Initial results from the Magellan stereo experiment, *J. of Geophys. Res.*, 97, 13675-13689.

Leberl, F.W., K. Maurice, J. Thomas, W. Kober (1991) Radargrammetric measurements from the initial Magellan coverage of planet Venus, *Photog. Engineering & Rem. Sens.*, 57, 1561-1570.

Leberl, F. (1990) *Radargrammetric Image Processing*. Artech House, Inc.

Muhleman, D.O. (1964) Radar scattering from Venus and the Moon, *Astron. J.*, v. 69, 34-41.

Pettengill, G.H., P.G. Ford, et. al. (1991) Magellan: Radar performance and data products, *Science*, 260-265.

Rice, S.O. (1951), Reflection of electromagnetic waves by slightly rough surfaces, Theory og Electromagnetic Wavess, ed. M. Kline, 351-378 (Interscience Publ., Inc., New York, N.Y.; Dover Publ., Inc., New York, N.Y.).

Rignot, E., P. Dubois, J. van Zyl (1992) The effect of topography on the estimation of geophysical parameters from airborne SAR data. Submitted to IEEE Trans. on Geosc. and Rem. Sens.

Schanda, E. (1985) A radargrammetry experiment in a mountain region, *Int. J. Remote Sensing*, 6, 1113-1124.

Senske, D.A., G.G. Schaber, E.R. Stofan (1992) Regional topographic rises on Venus: Geology of western Eistla Regio and comparison to Beta Regio and Atla Regio, *J. Geophys. Res.*, 97, 13395-13420.

Thomas, J., W. Kober, F. Leberl (1991) Multiple image SAR shape-from-shading, *Photog. Eng. & Rem. Sens.*, 57, 51-59.

Tyler, G.L., R.A. Simpson, et al. (1992) Scattering properties of the Venusian surface: preliminary results from Magellan, *J. of Geophys. Res.*, 97, 13115-13139.

Ulaby, F.T., R.K. Moore, A.K. Fung (1986) *Microwave Remote Sensing - Active and Passive*, Artech House Inc.

van Zyl, J.J., C.F. Burnette, T.G. Farr (1991) Inference of surface power spectra from inversion of multifrequency polarimetric radar data, *Geophys. Res. Letters*, 18, 1787-1790.

Vexcel Corporation (1994) *Magellan Stereo Toolkit User Manual.*

Welch R., D. Papacharalampos (1992) Three-dimensional terrain visualization on personal computers: An application with stereo SIR-B images, *Photog. Eng. & Rem. Sens.*, 58, 71-75.

Wildey, R. (1978), Radarclinometry for the Venus Radar Mapper, *Photog. Eng. and Remote Sensing*, Vol. LII, No. 1.

Zhang, Z., R. Deriche, O. Faugeras, Q. Luong, A robust technique for matching two uncalibrated images through the recovery of the unknown epipolar geometry, NRIA Report.

Additional Reading:

Arvidson, R.E., R. Greeley, et al. (1992a) Surface modification of Venus as inferred from Magellan observations of plains, *J. Geophys. Res.*, 97, 13303-13317.

Barrick, D.E. (1968) Rough surface scattering based on the specular point theory, *IEEE Trans. on Antennas and Propagation*, AP-16, 449-454.

Barrick, D.E., W.H. Peake (1968) A review of scattering from surfaces with different roughness scales, *Radio Science*, 3, 865-868.

Beckmann, P., A. Spizzichino (1963) *The scattering of electromagnetic waves from rough surfaces*, Pergamon Press.

Bindschadler, D.L., J.W. Head (1989) Characterization of venera 15/16 geologic units from pioneer Venus reflectivity and roughness data. *ICARUS*, 77, 3-20.

Bindschadler, D.L., J.W. Head (1988) Diffuse scattering of radar on the surface of Venus: Origin and implications for the distribution of soils. *Earth, Moon and Planets*, 42, 133-149.

Blom, R.G. (1988) Effects of variation in look angle and wavelength in radar images of volcanic and aeolian terrains, or Now you see it, now you don't, *Int. J. Remote Sensing*, 9, 945-965.

Burrough, P.A. (1981) Fractal dimensions of landscapes and other environmental data, *Nature*, 294, 240-242.

Campbell, B.A., S.H. Zisk, P.J. Mouginis-Mark (1989) A quad-pol radar scattering model for use in remote sensing of lava flow morphology. *Remote Sensing Environ.*, 30, 227-237.

Curlander, J.C., R. McDonough (1991) *Synthetic aperture radar*. John Wiley & Sons, Inc.

Engman, E.T., J.R. Wang (1987) Evaluating roughness models of radar backscatter. *IEEE Trans. of Geosc. and Rem. Sens.*, GE-25, 709-713.

Fleischmann, M., D.J. Tildesley, R.C. Ball (1989) Fractals in the Natural Sciences Princeton University Press.

Fox, C.G., D.E. Hayes (1985) Quantitative methods for analyzing the roughness of the seafloor, *Rev. Geophys.*, 23, 1-48.

Hinse, M., Q.H.J. Gwyn, F. Bonn (1988) Radiometric correction of C-band imagery for topographic effects in regions of moderate relief. *IEEE Trans. on Geos. and Rem. Sens.*, 26, 122-132.

Holcomb, R.T. (1987) Eruptive history and long-term behavior of Kilauea Volcano, U.S. Geological Survey Prof. Paper, 1350, 261-350.

Huang, J., D.L. Turcotte (1990) Fractal image analysis: Application to the topography of Oregon and synthetic images, *J. Opt. Soc. Am., A. Opt. Image Sci.*, 7, 1124-1130.

Huang, J., D.L. Turcotte (1989) Fractal mapping of digitized images: Application to the topography of Arizona and comparisons with synthetic images. *J. of Geophys. Res.*, 94, 7491-7495.

Jin, M.Y. (1990) Definition and generation of SDPS processing parameters.

Klose, K.B., J.A. Wood, A. Hashimoto (1992) Mineral equilibria and the high radar reflectivity of Venus mountaintops. *J. of Geophys. Res.* 97, 16353-16369.

Kodis, R.D. (1966) A note on the theory of scattering from an irregular surface. *IEEE Trans. on Antennas and Propagation*, 14, 77-82.

Kucinskas, A.B., D.L. Turcotte, J. Huang, et al. (1992) Fractal analysis of Venus topography in Tinatin Planitia and Ovda Regio, *J. Geophy. Res.*, 97, 13635-13641.

Kuntz, M.A., E.C. Spiker, et al. Radiocarbon studies of latest Pleistocene and Holocene lava flows of the Snake River Plain, Idaho: Data, lessons, interpretations, *Quat. Res.*, 25, 163-176.

Malin, M.C., D. Dzurisin, R.P. Sharp (1983) Stripping of Keanakakoi tephra on Kilauea Volcano, Hawaii, *Geol. Soc. Amer. Bull.*, 94, 1148-1158.

Papson, R.P. (1977) Geological guide to Craters of the Moon National Monument, In *Volcanism of the Eastern Snake River Plain, Idaho: A Comparative Planetary Geology Guidebook*, R. Greeley and J.S. King, eds., NASA CR-154621, 216-232.

Sayles, R.S., T.R. Thomas (1978) Surface topography as a nonstationery random process, *Nature*, 271, 431-434.

Solomon, S.C., J.W. Head (1991) Fundamental issues in the geology and geophysics of Venus, *Science*, 252, 252-260.

Turrin, B.D., J.C. Dohrenwend (1984) K-Ar ages of basaltic volcanism in the Lunar Crater volcanic field, northern Nye County, Nevada, *Geol. Soc. Amer. Abs. with Prog.*, 16, 679.

Tyler, G.L., P.G. Ford, D.B. Campbell, et al., (1991) Magellan: Electrical and physical properties of Venus' surface, *Science*, 252, 265-270.

Wall, S.D., T.G. Farr (1991) Measurement of surface microtopography, *Photog. Eng. & Rem. Sens.*, 57, 1075-1078.

REPORT DOCUMENTATION PAGE

Form Approved
OMB No. 0704-0188

1. AGENCY USE ONLY (Leave blank)	2. REPORT DATE	3. REPORT TYPE AND DATES COVERED
	Sep 94	Interim

4. TITLE AND SUBTITLE
Venus Surface Roughness and Magellan Stereo Data

5. FUNDING NUMBERS
C NASW-4854

6. AUTHOR(S)
Kelly Maurice, Franz Leberl, Scott Hensley

7. PERFORMING ORGANIZATION NAME(S) AND ADDRESS(ES)
Vexcel Corporation, 2477 55th Street, Suite #201, Boulder, Colorado 80301

8. PERFORMING ORGANIZATION REPORT NUMBER
VDAP-R1

9. SPONSORING/MONITORING AGENCY NAME(S) AND ADDRESS(ES)
NASA Headquarters, HQ Acquisition Division, Attention Todd Weber, Washington, DC 20546

10. SPONSORING/MONITORING AGENCY REPORT NUMBER
NA

11. SUPPLEMENTARY NOTES
Prepared in cooperation with Jet Propulsion Laboratory and California Institute of Technology.

12a. DISTRIBUTION/AVAILABILITY STATEMENT

12b. DISTRIBUTION CODE

13. ABSTRACT (Maximum 200 words)

Presented are results of some studies to develop tools useful for the analysis of Venus surface shape and of its roughness. Actual work was focused on Maxwell Montes. The analyses employ data acquired by means of NASA's Magellan satellite. The work is primarily concerned with deriving measurements of the Venusian surface using Magellan stereo SAR. Roughness was considered by means of a theoretical analyses based on Digital Elevation Models (DEMs), on single Magellan radar images combined with radiometer data, and on the sue of multiple overlapping Magellan radar images from Cycles I, II and III, again combined with collateral radiometer data.

14. SUBJECT TERMS
Radargrammetry, surface roughness, stereo SAR

15. NUMBER OF PAGES

16. PRICE CODE

17. SECURITY CLASSIFICATION OF REPORT	18. SECURITY CLASSIFICATION OF THIS PAGE	19. SECURITY CLASSIFICATION OF ABSTRACT	20. LIMITATION OF ABSTRACT
Unclassified	Unclassified	Unclassified	